# A Novel Transformation of the Ice Sheet Stokes Equations and Some of its Properties and Applications

John K. Dukowicz

Guest Scientist, Group T-3, Los Alamos National Laboratory,

Los Alamos, New Mexico, 87545, USA

*Correspondence to:* John K. Dukowicz (jn.dk@outlook.com)

**Abstract.**     We introduce a novel transformation of the Stokes equations into a form closely resembling the shallow Blatter-Pattyn equations. The two forms differ by only a few additional terms, while their variational formulations differ only by a single term in each horizontal direction. Specifically, the variational formulation of the Blatter-Pattyn model drops the vertical velocity in the second invariant of the strain rate tensor. Here we make use of the new transformation in two ways. First, we consider incorporating the transformed equations into a code that can be very easily converted from a Stokes to a Blatter-Pattyn model, and vice-versa, by switching these terms on or off. This may be generalized so that the Stokes model is switched on adaptively only where the Blatter-Pattyn model loses accuracy. Second, the key role played by the vertical velocity in the Blatter-Pattyn approximation motivates new approximations. Two examples are presented. These require a mesh that enables the discrete continuity equation to be invertible for the vertical velocity in terms of the horizontal velocity components. Examples of such meshes, such as the first order P1-E0 mesh and the second order P2-E1 mesh are given in both 2D and 3D. However, the transformed Stokes model has the same type of gravity forcing as the Blatter-Pattyn model, determined by the ice surface slope, thereby forgoing some of the mesh-generality of the traditional formulation of the Stokes model.

## 1 Introduction

Concern and uncertainty about the magnitude of sea level rise due to melting of the Greenland and Antarctic ice sheets have led to increased interest in improved ice sheet and glacier modeling. The gold standard is a Stokes model (i.e., a model that solves the nonlinear, non-Newtonian Stokes system of equations for incompressible ice sheet dynamics) because it is applicable to all geometries and flow regimes. However, the Stokes model is computationally demanding. It is a nonlinear, three-dimensional model involving four variables, namely, the three velocity components and pressure. The pressure is a Lagrange multiplier enforcing incompressibility and this creates a more

38    difficult indefinite "saddle point" problem. As a result, full-Stokes models exist but are

39    not commonly used in practice (examples are FELIX-S, Leng et al., 2012; Elmer/Ice,

40    Gagliardini et al., 2013).

42        Because of this there is much interest in simpler and cheaper approximate models.

43    There is a hierarchy of very simple models, such as the shallow ice (SIA) and shallow-

44    shelf (SSA) models, and there are also more accurate higher-order approximations.

45    These culminate in the Blatter-Pattyn (BP) approximation (Blatter, 1995; Pattyn, 2003),

46    which is currently used in production code packages such as ISSM (Larour et al., 2012),

47    MALI (Hoffman et al., 2018; Tezaur et al., 2015) and CISM (Lipscomb et al., 2019).

48    This approximation is based on the assumption of a small ice sheet aspect ratio, i.e.,

49    $\varepsilon = H/L \ll 1$, where $H, L$ are the vertical and horizontal length scales, and consequently

50    it eliminates certain stress terms and implicitly assumes small basal slopes. Both the

51    Stokes and Blatter-Pattyn models are described in detail in Dukowicz et al. (2010),

52    hereafter referred to as DPL (2010). Although the Blatter-Pattyn model is reasonably

53    accurate for large-scale motions, accuracy deteriorates for small horizontal scales, less

54    than about five ice thicknesses in the ISMIP–HOM model intercomparison (Pattyn et al.,

55    2008; Perego et al., 2012), or below a 1 km resolution as found in a detailed comparison

56    with full Stokes calculations (Rückamp et al, 2022). This can become particularly

57    important for calculations involving details near the grounding line where the full

58    accuracy of the Stokes model is needed (Nowicki and Wingham, 2008). Attempts to

59    address the problem while avoiding the use of full Stokes solvers include variable mesh

60    resolution coupled with a Blatter-Pattyn solver (Hoffman et al., 2018) and variable model

61    complexity, where a Stokes solver is embedded locally in a lower order model (Seroussi

62    et al., 2012). Approximations that are more accurate than Blatter-Pattyn but cheaper than

63    Stokes are currently not available.

64

65        The present paper introduces two innovations that may begin to address some of

66    these issues. The first is a novel transformation of the Stokes model, described in §3,

67    which puts it into a form closely resembling the Blatter-Pattyn model and differing only

68    by the presence of a few extra terms. This allows a code to be switched over from Stokes

69    to Blatter-Pattyn, and vice-versa, globally or locally, by the use of a single parameter that

70    turns off these extra terms thus enabling variable model complexity to be very simply

71    implemented as described in §6.1. The second innovation is the introduction of new

May 17, 2025

72 finite element discretizations that decouple the discrete continuity equation and allow it to

73 be solved for the vertical velocity in terms of the horizontal velocity components.

74 Several elements used to construct such meshes are described in Appendix A in both 2D

75 and 3D, primarily the first order P1-E0 and second order P2-E1 elements (these two

76 elements are novel and are so-named because they employ pressures located on vertical

77 mesh edges). Within the framework of the transformed Stokes model these meshes

78 enable new approximations that surpass the Blatter-Pattyn approximation. We describe

79 two such approximations in §6.2. There is another very significant benefit. These new

80 meshes allow Stokes ice sheet models to be converted into inherently stable

81 unconstrained minimization problems without invoking the "inf-sup" condition as shown

82 in §4.3.2.

83

84 **2 The Standard Formulation of the Stokes Ice Sheet Model**

85 **2.1 The Assumed Ice Sheet Configuration**

86

87 An ice sheet may be divided into two parts, a part in contact with the bed and a floating

88 ice shelf located beyond the grounding line. The Stokes ice sheet model is capable of

89 describing the flow of an arbitrarily shaped ice sheet, including a floating ice shelf as

90 illustrated in Fig. 1, given appropriate boundary conditions (e.g., Cheng et al., 2020).

91 One limitation of the methods proposed here, in common with the Blatter-Pattyn model,

92 will be that there should be just one upper and one basal surface, as is the case in Fig. 1.

93 For simplicity we only consider fully grounded ice sheets with periodic lateral boundary

94 conditions although ice shelves can be incorporated.
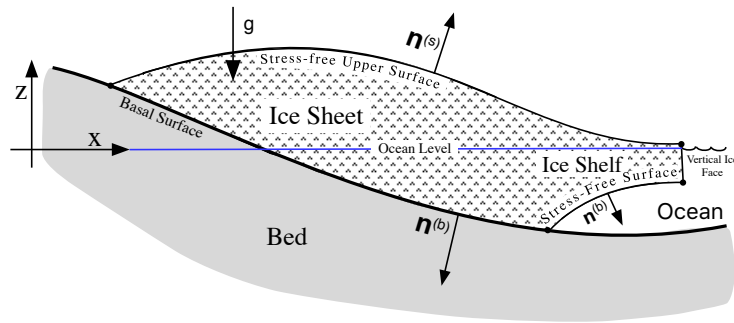
95
96
97         **Figure 1** A simplified illustration of the admissible ice sheet configuration.

98

May 17, 2025

99       Referring to Fig. 1, the entire surface of the ice sheet is denoted by $S$. An upper

100   surface, labeled $S_s$ and specified by $\varsigma_s(x,y,z)=z-z_s(x,y)=0$, is exposed to the

101   atmosphere and thus experiences stress-free boundary conditions. The bottom or basal

102   surface, denoted by $S_B$ and specified by $\varsigma_b(x,y,z)=z-z_b(x,y)=0$, is in contact with

103   the bed. The basal surface may be subdivided into two sections, $S_B = S_{B1} \cup S_{B2}$, where

104   $S_{B1}$, specified by $z=z_{b1}(x,y)$, is the part where ice is frozen to the bed (a no-slip

105   boundary condition), and $S_{B2}$, specified by $z=z_{b2}(x,y)$, is where frictional sliding

106   occurs. We assume Cartesian coordinates such that $x_i = (x,y,z)$ are position coordinates

107   with $z=0$ at the ocean surface, and the index $i \in \{x,y,z\}$ represents the three Cartesian

108   indices. Later we shall have occasion to introduce the restricted index $(i) \in \{x,y\}$ to

109   represent just the two horizontal indices. This is more compact than the equivalent

110   projection operator, i.e., $u_{(i)} = P_i(u) = (u,v,0)$. Unit normal vectors appropriate for the

111   ice sheet configuration of Fig. 1 are given by

$$n_i = (n_x, n_y, n_z) = \frac{\partial \varsigma_s(x,y,z)/\partial x_i}{|\partial \varsigma_s(x,y,z)/\partial x_i|} = \frac{(-\partial z_s/\partial x, -\partial z_s/\partial y, 1)}{\sqrt{1+(\partial z_s/\partial x)^2+(\partial z_s/\partial y)^2}} \quad \text{at surface } S_S,$$

112 $$\hspace{11cm}(1)$$

$$n_i = (n_x, n_y, n_z) = -\frac{\partial \varsigma_b(x,y,z)/\partial x_i}{|\partial \varsigma_b(x,y,z)/\partial x_i|} = \frac{(\partial z_b/\partial x, \partial z_b/\partial y, -1)}{\sqrt{1+(\partial z_b/\partial x)^2+(\partial z_b/\partial y)^2}} \quad \text{at surface } S_B.$$

113

114 **2.2 The Stokes Equations**

115

116 The Stokes model is a system of nonlinear partial differential equations and associated

117 boundary conditions (Greve and Blatter, 2009; DPL, 2010). In Cartesian coordinates the

118 Stokes equations, the three momentum equations and the continuity equation for the three

119 velocity components $u_i = (u,v,w)$ and the pressure $P$, are given by

120 $$\frac{\partial \tau_{ij}}{\partial x_j} - \frac{\partial P}{\partial x_i} + \rho g_i = 0, \hspace{5cm} (2)$$

121 $$\frac{\partial u_i}{\partial x_i} = 0, \hspace{6cm} (3)$$

122 where $\rho$ is the density, and $g_i$ is the acceleration vector due to gravity, arbitrarily

123 oriented in general but here taken to be in the negative z-direction, $g_i = (0,0,-g)$.

124 Repeated indices imply summation (the Einstein notation). The deviatoric stress tensor

125 $\tau_{ij}$ is given by

$$\tau_{ij} = 2\mu_n \dot{\varepsilon}_{ij} , \tag{4}$$

127 where the strain rate tensor is

$$\dot{\varepsilon}_{ij} = \frac{1}{2}\left(\frac{\partial u_i}{\partial x_j} + \frac{\partial u_j}{\partial x_i}\right), \tag{5}$$

129 the nonlinear ice viscosity $\mu_n$ is

$$\mu_n = \eta_0 \left(\dot{\varepsilon}^2\right)^{(1-n)/2n} , \tag{6}$$

131 and $\dot{\varepsilon}^2 = \dot{\varepsilon}_{ij}\dot{\varepsilon}_{ij}/2 \geq 0$ is the second invariant of the strain rate tensor that may be written

132 out in full as follows

$$\dot{\varepsilon}^2 = \frac{1}{2}\left[\left(\frac{\partial u}{\partial x}\right)^2 + \left(\frac{\partial v}{\partial y}\right)^2 + \left(\frac{\partial w}{\partial z}\right)^2\right] + \frac{1}{4}\left[\left(\frac{\partial u}{\partial y} + \frac{\partial v}{\partial x}\right)^2 + \left(\frac{\partial u}{\partial z} + \frac{\partial w}{\partial x}\right)^2 + \left(\frac{\partial v}{\partial z} + \frac{\partial w}{\partial y}\right)^2\right]. \tag{7}$$

134 As usual, ice is assumed to obey Glen's flow law, where $n$ is the Glen's law exponent

135 ($n = 1$ for a linear Newtonian fluid but typically $n = 3$ in ice sheet modeling, describing a

136 nonlinear non-Newtonian fluid). The coefficient $\eta_0$ is defined by $\eta_0 = A^{-1/n}/2$, where

137 $A$ is an ice flow factor, in general depending on temperature and other variables (see

138 Schoof and Hewitt, 2013) but here taken to be a constant. The three-dimensional Stokes

139 system requires a set of boundary conditions at every bounding surface, each set

140 composed of three components. Aside from the periodic lateral boundary conditions, the

141 relevant boundary conditions are given as follows

142     (1) Stress-free boundary conditions on surfaces $S_S$ not in contact with the bed, such

143 as the upper surface $S_S$:

$$\tau_{ij}n_j - Pn_t = 0 . \tag{8}$$

145     (2) No-slip or frozen to the bed conditions on surface segment $S_{B1}$:

$$u_i = 0 . \tag{9}$$

147     (3) Frictional tangential sliding conditions on surface segment $S_{B2}$:

May 17, 2025

148    We assume that the tangential frictional shear force that resists sliding, $\tau_i^S$, is a known

149    vector that satisfies the no-penetration condition, $\tau_i^S n_i = 0$. Note that only two

150    components need to be provided since the third may always be obtained from the

151    tangency condition. In general $\tau_i^S$ is a complicated function of position and velocity

152    (e.g., Schoof, 2010). At a surface where frictional sliding takes place the flow velocity

153    must be tangential to the surface, satisfying

154    $$u_i n_i = 0. \tag{10}$$

155    Following DPL (2010), the tangential stress balance at the basal surface is given by

156    $$\tau_{ij} n_j - \tau_n n_i + \tau_i^S = 0, \tag{11}$$

157    where $\tau_n = n_i \tau_{ij} n_j$ is the normal component of the shear stress. However, the three

158    components of the stress balance (11) are not independent since the stress balance vector

159    is confined to the tangential plane. Thus, choosing the horizontal components of (11) as

160    the two independent components, the required three boundary conditions are given by the

161    no-penetration condition (10) and the two horizontal components of (11), namely

162    $$\tau_{(i)j} n_j - \tau_n n_{(i)} + \tau_{(i)}^S = 0. \tag{12}$$

163    In this paper we shall assume simple linear frictional sliding, given by

164    $$\tau_i^S = \beta(x) u_i, \tag{13}$$

165    where $\beta(x) > 0$ is a position-dependent drag law coefficient. We also assume that there

166    is no melting or refreezing at the bed, causing vertical inflows or outflows. If needed,

167    these can be easily added to (10) (see Dukowicz et al., 2010; Heinlein et al., 2022).

168

169    **2.3 The Stokes Variational Principle**

170

171    A variational principle, if available, is the most compact way of representing a particular

172    problem. It is fortunate that the Stokes model possesses a variational principle that is

173    particularly useful for discretization and for the specification of boundary conditions (see

174    Colinge and Rappaz (1999), Rappaz and Reist (2005) for early use of the variational

175    principle in glaciology, and Schoof (2006), DPL (2010) for a fuller description of the

176    variational principle as applied in ice sheet modeling). There are a number of significant

177    advantages. For example, all boundary conditions are conveniently incorporated in the

178    variational formulation, terms in the variational functional generally contain lower order

179 derivatives, and the discretization automatically generates a symmetric matrix. Stress
180 terms are evaluated in the interior thereby avoiding the need to evaluate derivatives using
181 less accurate one-sided approximations at boundaries. Stress-free boundary conditions,
182 as at the upper surface, need not be specified at all since they are automatically
183 incorporated in the functional as natural boundary conditions. Finally, functional
184 variation in the discrete case is equivalent to simple differentiation with respect to the
185 discrete variables as demonstrated in §4. The variational method presented here is
186 closely related to the Galerkin method, a subset of the weak formulation method in finite
187 elements in which the test and trial functions are the same (see Schoof, 2010, and earlier
188 references contained therein in connection with the Blatter-Pattyn model).
189
190 The variational functional for the standard Stokes model may be written in two
191 alternative forms:
192 (1) Basal boundary conditions imposed using Lagrange multipliers:

$$\mathcal{A}[u_i, P, \lambda_i, \Lambda] = \int_V dV \left[ \frac{4n}{n+1} \eta_0 \left( \dot{\varepsilon}^2 \right)^{(1+n)/2n} - P \frac{\partial u_i}{\partial x_i} + \rho g w \right]$$
$$+ \int_{S_{B1}} dS \, \lambda_i u_i + \int_{S_{B2}} dS \left[ \Lambda u_i n_i + \frac{1}{2} \beta(x) \, u_i u_i \right], \tag{14}$$

194 where $\lambda_i$ and $\Lambda$ are Lagrange multipliers used to enforce the no-slip condition and
195 frictional tangential sliding, respectively. As in DPL (2010), arguments enclosed in
196 square brackets, here $u_i, P, \lambda_i, \Lambda$, indicates the functions that are subject to variation.
197 (2) Basal boundary conditions imposed by direct substitution:
198 In case of no-slip conditions, condition (9) is used directly in the functional to zero out all
199 velocity components $u_i$ along the $S_{B1}$ section of the basal boundary. In case of
200 tangential sliding, the functional is given by

$$\mathcal{A}[u_i, P] = \int_V dV \left[ \frac{4n}{n+1} \eta_0 \left( \dot{\varepsilon}^2 \right)^{(1+n)/2n} - P \frac{\partial u_i}{\partial x_i} + \rho g w \right]$$
$$+ \frac{1}{2} \int_{S_{B2}} dS \, \beta(x) \left( u_{(i)} u_{(i)} + \left( u_{(i)} n_{(i)} / n_z \right)^2 \right), \tag{15}$$

202 where, using the tangential sliding condition (10), the velocity along the entire basal
203 boundary section $S_{B2}$ is specified by

$$u_i = \left( u, v, -u_{(i)} n_{(i)} / n_z \right) = \left( u, v, u_{(i)} \partial z_b / \partial x_{(i)} \right). \tag{16}$$

May 17, 2025

205    This is implicitly done in all terms of the functional, i.e., the volume integral terms as

206    well as the surface integral term, in which case the replacement is explicitly visible in

207    (15). This use of (16) to replace the relevant surface velocities in the functional is

208    sufficient to implement the tangential sliding boundary condition. The replacement is

209    particularly easy in the discrete formulation, to be described later, where boundary or

210    surface velocity variables are easily accessible for replacement.

211

212        As fully described in DPL (2010), a variational procedure yields the full set of

213    Euler-Lagrange equations and boundary conditions that specify the standard Stokes

214    model, equivalent to (2)-(12). In the case of (14), the discrete variational procedure

215    determines the discrete variables that specify the velocity components and the pressure,

216    $u_i, P$ , and the Lagrange multipliers, $\lambda_i, \Lambda$ . In the direct substitution case, (15), the

217    solution determines only the discrete pressures $P$ and velocity variables $u_i$ that were not

218    directly prescribed as boundary conditions in (9) or (16). These prescribed (known)

219    values of boundary velocities are then added a posteriori to obtain the complete set of

220    discrete variables. The direct substitution method is smaller, simpler, and is therefore

221    more commonly used in this paper.

222

223    **3. A Transformation of the Stokes Model**

224    **3.1 Origin of the Transformation**

225

226    The transformation is motivated by the Blatter-Pattyn approximation. Consider the

227    vertical component of the momentum equation and the corresponding stress-free upper

228    surface boundary condition in the Blatter-Pattyn approximation (from DPL, 2010, for

229    example), which are given by

230

$$\frac{\partial}{\partial z}\left(2\mu_n \frac{\partial w}{\partial z}\right) - \frac{\partial P}{\partial z} - \rho g = 0,$$

$$\left(2\mu_n \frac{\partial w}{\partial z} - P\right)n_z = 0 \quad \text{at} \quad z = z_s(x,y).$$

(17)

231    These equations suggest the use of a new variable $\tilde{P}$ , to be called the transformed

232    pressure, given by

233

$$\tilde{P} = P - 2\mu_n \frac{\partial w}{\partial z} + \rho g\left(z - z_s(x,y)\right).$$

(18)

234    Substituting, this simplifies (17) as follows

May 17, 2025

$$\frac{\partial \tilde{P}}{\partial z} = 0, \tag{19}$$
$$\tilde{P} n_z = 0 \quad \text{at} \quad z = z_s(x, y),$$

236 which is a complete one-dimensional partial differential system yielding

$$\tilde{P} = 0 \tag{20}$$

238 when integrated from the top surface down. Thus, the transformed pressure vanishes in
239 the Blatter-Pattyn case. The definition (18) forms the basis of the present transformation
240 but we also use the continuity equation to eliminate $\partial w/\partial z$ as in the Blatter-Pattyn
241 approximation (e.g., Pattyn, 2003). Therefore, the transformation consists of eliminating
242 $P$ and $\partial w/\partial z$ in the Stokes system (2), (4)-(12) (i.e., everywhere except in the
243 continuity equation (3) itself) by means of

$$P = \tilde{P} - 2\mu_n \left( \frac{\partial u}{\partial x} + \frac{\partial v}{\partial y} \right) + \rho g (z_s - z), \tag{21}$$

$$\frac{\partial w}{\partial z} = -\left( \frac{\partial u}{\partial x} + \frac{\partial v}{\partial y} \right). \tag{22}$$
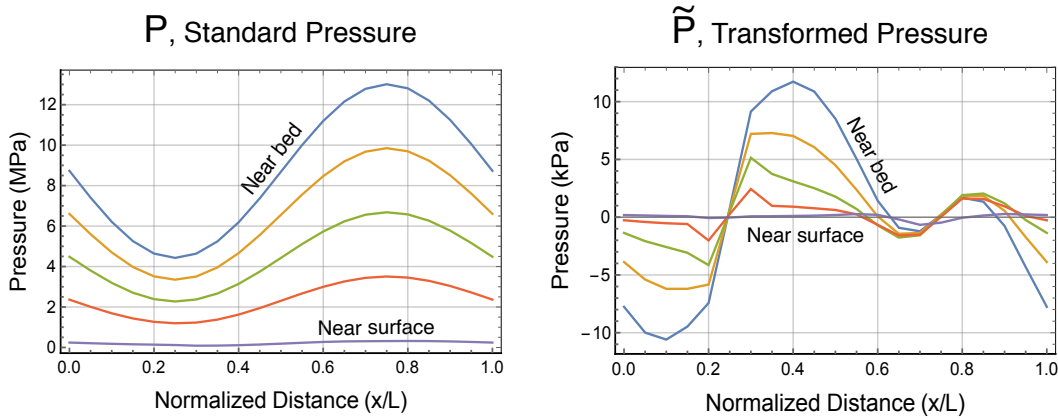
247 **Figure 2.** Standard pressure $P$ (MPa) compared to the transformed pressure $\tilde{P}$ (kPa) in
248 Exp. B from the ISMIP–HOM model intercomparison (Pattyn et al., 2008) at L = 10 km.

250     The pressure P in the standard Stokes system is primarily a Lagrange multiplier
251 enforcing incompressibility, but with a very large hydrostatic component. The
252 transformation eliminates the hydrostatic pressure from $\tilde{P}$, as illustrated in Fig. 2 where
253 the two pressures are compared. Thus, the transformed pressure $\tilde{P}$ is some three orders
254 of magnitude smaller than $P$ primarily because of the absence of hydrostatic pressure.

May 17, 2025

256     The transformed pressure $\tilde{P}$ again acts as a Lagrange multiplier enforcing

257     incompressibility. Since $\tilde{P} = 0$ in the Blatter-Pattyn approximation, the transformed

258     pressure may be written as $\tilde{P} = P - P_{BP}$, where

259
$$P_{BP} = -2\mu_n \left( \frac{\partial u}{\partial x} + \frac{\partial v}{\partial y} \right) + \rho g \left( z_s - z \right)$$

260     is the effective Blatter-Pattyn pressure (Tezaur et al., 2015). Thus, $P = P_{BP} + \tilde{P}$ and

261     therefore $\tilde{P}$ can be interpreted as the "Stokes" correction to the Blatter-Pattyn pressure.

262

263     **3.2 The Transformed Stokes Equations**

264

265     Introducing (21), (22) into the Stokes system of equations (2)-(12) results in the

266     following transformed Stokes system:

267
$$\frac{\partial \tilde{\tau}_{ij}}{\partial x_j} - \hat{\xi} \frac{\partial \tilde{P}}{\partial x_i} - \rho g \frac{\partial z_s}{\partial x_{(i)}} = 0 ,$$
(23)

268
$$\hat{\xi} \frac{\partial u_i}{\partial x_i} = 0 ,$$
(24)

269     where quantities modified in the transformation are indicated by a tilde, e.g., $\tilde{P}$.

270     Corresponding to (4), the modified Stokes deviatoric stress tensor $\tilde{\tau}_{ij}$ is given by

271
$$\tilde{\tau}_{ij} = \tilde{\mu}_n \begin{bmatrix} 2\left( 2\frac{\partial u}{\partial x} + \frac{\partial v}{\partial y} \right) & \left( \frac{\partial u}{\partial y} + \frac{\partial v}{\partial x} \right) & \left( \frac{\partial u}{\partial z} + \xi\frac{\partial w}{\partial x} \right) \\ \left( \frac{\partial u}{\partial y} + \frac{\partial v}{\partial x} \right) & 2\left( \frac{\partial u}{\partial x} + 2\frac{\partial v}{\partial y} \right) & \left( \frac{\partial v}{\partial z} + \xi\frac{\partial w}{\partial y} \right) \\ \xi\left( \frac{\partial u}{\partial z} + \frac{\partial w}{\partial x} \right) & \xi\left( \frac{\partial v}{\partial z} + \frac{\partial w}{\partial y} \right) & 0 \end{bmatrix} ,$$
(25)

272     Dummy variables $\xi, \hat{\xi}$ (here assumed to be $\xi, \hat{\xi} = 1$) are used in (23)-(25) to indicate

273     terms that are absent in the Blatter-Blatter approximation as will be explained below.

274     The modified viscosity $\tilde{\mu}_n$, corresponding to (6), is given by

275
$$\tilde{\mu}_n = \eta_0 \left( \tilde{\dot{\varepsilon}}^2 \right)^{(1-n)/2n} ,$$
(26)

276     where the transformed second invariant $\tilde{\dot{\varepsilon}}^2$, corresponding to (7), is

May 17, 2025

277
$$\tilde{\dot\varepsilon}^2 = \left(\frac{\partial u}{\partial x}\right)^2 + \frac{\partial u}{\partial x}\frac{\partial v}{\partial y} + \left(\frac{\partial v}{\partial y}\right)^2 + \frac{1}{4}\left[\left(\frac{\partial u}{\partial y}+\frac{\partial v}{\partial x}\right)^2 + \left(\frac{\partial u}{\partial z}+\xi\frac{\partial w}{\partial x}\right)^2 + \left(\frac{\partial v}{\partial z}+\xi\frac{\partial w}{\partial y}\right)^2\right]. \quad (27)$$

278    Since (27) differs from (7) only by the incorporation of the continuity equation (22), the

279    transformation leaves both the second invariant $\tilde{\dot\varepsilon}^2$ and viscosity $\tilde\mu_n$ unchanged, i.e.,

280    $\tilde{\dot\varepsilon}^2 = \dot\varepsilon^2$ and $\tilde\mu_n = \mu_n$. The second invariant remains non-negative, i.e., $\tilde{\dot\varepsilon}^2 \geq 0$.

281

282        Boundary conditions for the transformed equations, corresponding to (8)-(12), are

283    given by

284    BCs on $S_S$:
$$\tilde\tau_{ij} n_j - \hat\xi \tilde P n_i = 0, \quad (28)$$

285    BCs on $S_{B1}$:
$$u_i = 0, \quad (29)$$

286    BCs on $S_{B2}$:
$$u_i n_i = 0, \quad (30)$$

287
$$\tilde\tau_{(i)j} n_j - \tilde\tau_n n_{(i)} + \beta(x) u_{(i)} = 0, \quad (31)$$

288    where $\tilde\tau_n = n_i \tilde\tau_{ij} n_j$ as before. Equations (30), (31) constitute the required three frictional

289    sliding boundary conditions.

290

291        As mentioned, dummy variables $\xi, \hat\xi$ in (23)-(25), (27), and (28) are used to

292    identify terms that are neglected in the two types of the Blatter-Pattyn approximation

293    discussed in §3.4. These are (a) the standard Blatter-Pattyn approximation, $\xi = 0, \hat\xi = 0$,

294    as originally derived (Blatter, 1995; Pattyn, 2003; DPL, 2010), which solves for just the

295    horizontal velocity components $u, v$, and (b) the extended Blatter-Pattyn approximation,

296    $\xi = 0, \hat\xi = 1$, described more fully later, that contains the standard approximation plus

297    additional equations that determine the vertical velocity $w$ and the pressure $\tilde P$. Keeping

298    all terms, i.e., $\xi = 1, \hat\xi = 1$, specifies the full transformed Stokes model.

299

300        The transformed system, (23)-(31), and the standard Stokes system, (2)-(12), yield

301    exactly the same solution. However, in common with the Blatter-Pattyn approximation,

302    the transformed system must use a gravity-oriented coordinate system because of the

303    particular type of gravitational forcing being used, while the standard Stokes model is not

304    similarly restricted. This is not a major limitation. A somewhat more restrictive

305  limitation is the appearance of $z_s(x,y)$, an implicitly single valued function, to describe

306  the vertical position of the upper surface of the ice sheet. This means that care must be

307  taken with reentrant upper surfaces (i.e., S-shaped in 2D) and sloping cliffs at an ice

308  edge, again a restriction that is not present in the standard Stokes model. As noted

309  previously, we assume that there is just one upper and one basal surface, i.e., as usual in

310  ice sheet modeling we do not permit overhangs.

311

312  **3.3 The Transformed Stokes Variational Principle**

313

314  It is easy to verify that the transformed Stokes system (23)-(31) results from the variation

315  with respect to $u_i, \tilde{P}$ of the following functional:

316
$$\tilde{\mathcal{A}}[u_i, \tilde{P}] = \int_V dV \left[ \frac{4n}{n+1} \eta_0 \left( \tilde{\varepsilon}^2 \right)^{(1+n)/2n} - \hat{\xi} \tilde{P} \frac{\partial u_i}{\partial x_i} + \rho g u_{(i)} \frac{\partial z_s}{\partial x_{(i)}} \right]$$
$$+ \frac{1}{2} \int_{S_{B2}} dS \, \beta(x) \left( u_{(i)} u_{(i)} + \left( u_{(i)} n_{(i)} / n_z \right)^2 \right),$$
(32)

317  where $\tilde{\varepsilon}^2$ is the transformed second invariant, (27). As in functional (15), basal

318  boundary conditions are imposed by direct substitution. However, boundary conditions

319  using Lagrange multipliers as in (14) are also possible.

320

321  **3.4 Two Forms of the Blatter-Pattyn Approximation**

322  **3.4.1 The Standard Blatter-Pattyn Approximation**

323

324  The standard Blatter-Pattyn approximation (originally introduced by Blatter, 1995,

325  Pattyn, 2003; later by DPL, 2010; Schoof and Hewitt, 2013) is obtained by setting

326  $\xi = \hat{\xi} = 0$ in the transformed system. This yields the Blatter-Pattyn variational,

327
$$\mathcal{A}_{BP}[u_{(i)}] = \int_V dV \left[ \frac{4n}{n+1} \eta_0 \left( \dot{\varepsilon}_{BP}^2 \right)^{(1+n)/2n} + \rho g u_{(i)} \frac{\partial z_s}{\partial x_{(i)}} \right]$$
$$+ \frac{1}{2} \int_{S_{B2}} dS \, \beta(x) \left( u_{(i)} u_{(i)} + \varsigma \left( u_{(i)} n_{(i)} / n_z \right)^2 \right),$$
(33)

328  and the second invariant $\dot{\varepsilon}_{BP}^2$, as follows

May 17, 2025

329
$$\dot{\varepsilon}^2_{BP} = \left(\frac{\partial u}{\partial x}\right)^2 + \frac{\partial u}{\partial x}\frac{\partial v}{\partial y} + \left(\frac{\partial v}{\partial y}\right)^2 + \frac{1}{4}\left[\left(\frac{\partial u}{\partial y} + \frac{\partial v}{\partial x}\right)^2 + \frac{\partial u}{\partial z}^2 + \frac{\partial v}{\partial z}^2\right],$$ (34)

330 in terms of horizontal velocity components $u, v$ only. The Euler-Lagrange equations and

331 boundary conditions are given by

332
$$\frac{\partial \tau^{BP}_{(i)j}}{\partial x_j} - \rho g \frac{\partial z_s}{\partial x_{(i)}} = 0; \quad \begin{cases} \tau^{BP}_{(i)j} n_j + \beta(x)\left(u_{(i)} + \zeta\left(u_{(j)}n_{(j)}/n_z\right)n_{(i)}/n_z\right) = 0 \\ \text{on } S_{B2}, \quad \tau^{BP}_{(i)j} n_j = 0 \text{ on } S_S, \quad u_{(i)} = 0 \text{ on } S_{B1}, \end{cases}$$ (35)

333 where the Blatter-Pattyn stress tensor $\tau^{BP}_{(i)j}$ is

334
$$\tau^{BP}_{(i)j} = \eta_0 \left(\dot{\varepsilon}^2_{BP}\right)^{(1-n)/2n}\begin{bmatrix} 2\left(2\dfrac{\partial u}{\partial x} + \dfrac{\partial v}{\partial y}\right) & \left(\dfrac{\partial u}{\partial y} + \dfrac{\partial v}{\partial x}\right) & \dfrac{\partial u}{\partial z} \\[2mm] \left(\dfrac{\partial u}{\partial y} + \dfrac{\partial v}{\partial x}\right) & 2\left(\dfrac{\partial u}{\partial x} + 2\dfrac{\partial v}{\partial y}\right) & \dfrac{\partial v}{\partial z} \end{bmatrix}.$$ (36)

335 Equations (35), (36) correspond to (23) and (25) in the transformed Stokes system. A

336 new dummy variable $\zeta$ has been introduced in (33) to identify the basal boundary term

337 normally dropped in the standard Blatter-Pattyn approximation $(\zeta = 0)$ but which was

338 restored $(\zeta = 1)$ in Dukowicz et al. (2011) to better represent arbitrary basal topography.

339

340       The Blatter-Pattyn model solves for the horizontal velocity components only. If

341 desired, the vertical velocity component $w$ may in principle be computed a posteriori by

342 means of the continuity equation. Finally, it is important to point out that the Blatter-

343 Pattyn system is numerically well behaved because the variational formulation amounts

344 to a convex optimization problem whose solution minimizes the functional (33).

345

346 **3.4.2 The Extended Blatter-Pattyn Approximation**

347

348 A second form of the Blatter-Pattyn approximation is obtained from the transformed

349 variational principle (32) by making the assumption,

350
$$\left\|\frac{\partial w}{\partial x}\right\| \ll \left\|\frac{\partial u}{\partial z}\right\|, \quad \left\|\frac{\partial w}{\partial y}\right\| \ll \left\|\frac{\partial v}{\partial z}\right\|,$$ (37)

351 and therefore neglecting $\partial w/\partial x, \partial w/\partial y$ in the transformed second invariant $\tilde{\varepsilon}^2$,

352 consistent with the original small aspect ratio approximation (Blatter, 1995; Pattyn, 2003;

May 17, 2025

353    DPL, 2010; Schoof and Hindmarsh, 2008). This corresponds to setting $\xi = 0, \hat{\xi} = 1$ in the

354    transformed Stokes model. In other words, we neglect $w$-velocity gradients but keep the

355    pressure term in the functional. This will be called the extended Blatter-Pattyn

356    approximation (EBP) because, in contrast to the standard Blatter-Pattyn approximation,

357    all the variables, i.e., $u, v, w, \tilde{P}$, are retained. Notably, assumption (37) is equivalent to

358    just setting $w = 0$ in the second invariant $\tilde{\dot{\varepsilon}}^2$ in the transformed Stokes model. This

359    aspect of the transformed Stokes model will be exploited later to obtain approximations

360    that improve on the Blatter-Pattyn approximation. Thus, the extended Blatter-Pattyn

361    functional is given by

362

$$\mathcal{A}_{EBP}[u_i, \tilde{P}] = \int_V dV \left[ \frac{4n}{n+1} \eta_0 \left( \dot{\varepsilon}_{BP}^2 \right)^{(1+n)/2n} - \tilde{P} \frac{\partial u_i}{\partial x_i} + \rho g u_{(i)} \frac{\partial z_s}{\partial x_{(i)}} \right]$$
$$+ \frac{1}{2} \int_{S_{B2}} dS \, \beta(x) \left( u_{(i)} u_{(i)} + \varsigma \left( u_{(i)} n_{(i)} / n_z \right)^2 \right), \tag{38}$$

363    and the Blatter-Pattyn second invariant $\dot{\varepsilon}_{BP}^2$ is given by (34). Taking the variation of the

364    functional, the system of extended Blatter-Pattyn Euler-Lagrange equations and their

365    boundary conditions is given by

366        (1) Variation with respect to $u_{(i)}$ yields the horizontal momentum equation:

367

$$\frac{\partial \tau_{(i)j}^{BP}}{\partial x_j} - \frac{\partial \tilde{P}}{\partial x_{(i)}} - \rho g \frac{\partial z_s}{\partial x_{(i)}} = 0; \left\{ \begin{array}{l} \tau_{(i)j}^{BP} n_j - \tilde{P} n_{(i)} = 0 \text{ on } S_S, \quad u_{(i)} = 0 \text{ on } S_{B1}, \\[2mm] \tau_{(i)j}^{BP} n_j + \beta(x) \left( u_{(i)} + \varsigma \left( u_{(k)} n_{(k)} / n_z \right) n_{(i)} / n_z \right) = 0 \\[2mm] \text{on } S_{B2}, \end{array} \right. \tag{39}$$

368    where $\tau_{(i)j}^{BP}$ is given by (36).

369        (2) Variation with respect to $w$ yields the vertical momentum equation:

370

$$-\frac{\partial \tilde{P}}{\partial z} = 0; \qquad \tilde{P} n_z = 0 \text{ on } S_S, \tag{40}$$

371        (3) Variation with respect to $\tilde{P}$ yields the continuity equation:

372

$$\frac{\partial w}{\partial z} + \frac{\partial u_{(i)}}{\partial x_{(i)}} = 0; \qquad w = 0 \text{ on } S_{B1}, \text{ or } w = -u_{(i)} n_{(i)} / n_z \text{ on } S_{B2}. \tag{41}$$

373    It is apparent that the vertical momentum equation system (40) is decoupled, yielding

374    $\tilde{P} = 0$ as already shown in §3.1. This effectively eliminates pressure from the horizontal

May 17, 2025

375    momentum equation (39), making it identical to the standard Blatter-Pattyn system (35),

376    i.e., a decoupled equation for the horizontal velocities $u_{(i)}$. As a result, having obtained

377    the horizontal velocities from (39), the continuity equation (41) may in principle be

378    solved for the vertical velocity $w$ (but see the comments following (42) regarding the

379    discrete case).

380

381         In summary, the extended Blatter-Pattyn model, (39)-(41), is equivalent to the

382    standard Blatter-Pattyn model, (35), for the horizontal velocities, $u, v$, but it also includes

383    two additional equations that determine the pressure $\tilde{P}$ and the vertical velocity $w$,

384    which are ignored in the standard Blatter-Pattyn approximation where only the horizontal

385    velocity is calculated. Because of this, we distinguish between the _Blatter-Pattyn model_

386    that solves for just the two horizontal velocities (i.e., the standard Blatter-Pattyn

387    approximation, (35)), and the _Blatter-Pattyn system_ that solves for all the variables (i.e.,

388    the extended Blatter-Pattyn approximation, (39)-(41)). Perhaps the main distinction

389    between the two, which may be important in some applications, is that the vertical

390    velocity in the Blatter-Pattyn system is calculated by solving the continuity equation (41)

391    once horizontal velocities $u, v$ are available on the same mesh as the horizontal

392    velocities, while in the Blatter-Pattyn model the calculation of vertical velocity is

393    completely decoupled and may be done on an unrelated mesh. In the continuous case the

394    solution for the vertical velocity can be done using the Leibniz's theorem,

395
$$w(u,v) = w_{z=z_b} - \int_{z_b}^{z} \frac{\partial u_{(i)}}{\partial x_{(i)}} dz' = u_{(i)} \frac{\partial z_b}{\partial x_{(i)}} - \int_{z_b}^{z} \frac{\partial u_{(i)}}{\partial x_{(i)}} dz' = -\frac{\partial}{\partial x_{(i)}} \int_{z_b}^{z} u_{(i)} dz' . \qquad (42)$$

396    Equation (42) may be used as the starting point for discretization. However, in the

397    following we shall instead discretize the continuity equation (41) by the use of special

398    finite element meshes as described in Appendix A.

399

400         Up to now we have only dealt with continuum properties of Stokes-type systems,

401    which are well behaved. However, this may not be so in the discrete case. The solution

402    of the discretized Stokes systems will depend on the choices that are made for the meshes

403    and for the finite elements that are to be used. These issues will be discussed next.

404

405 **4. Finite Element Discretization**

406 **4.1 Standard and Transformed Stokes Discretizations**

407

408 In practice, both traditional Stokes and Blatter-Pattyn models are discretized using finite

409 element methods (e.g., Gagliardini et al., 2013; Perego et al., 2012). We follow this

410 practice except that here the discretization starts from the Stokes variational principle.

411 This differs from standard finite element practice that starts from the Stokes equations

412 and converts them into weak (integral) form, which may not be equivalent to a variational

413 principle unless the Galerkin method is used. This has a number of advantages (see §2.3

414 and DPL, 2010). The following is a brief outline of the discretization. Additional details

415 are provided in Appendix A. For simplicity, we confine ourselves to two dimensions

416 with coordinates $(x,z)$ and velocities $(u,w)$. An example of a three-dimensional mesh

417 appropriate for our purpose is discussed in Appendix A. Further, we discuss only the

418 case of direct substitution for basal boundary conditions in the variational functional.

419 Note that remarks in this Section will apply to both the standard and the transformed

420 Stokes models; for example, the discrete pressure variable $p$ may refer to either the

421 standard pressure $P$ or the transformed pressure $\tilde{P}$.

422

423 Consider an arbitrary mesh with a total of $N = n_u + n_w + n_p$ unknown discrete

424 variables at nodal locations $1 \le i \le N$, with $n_u$ horizontal velocity variables, $n_w$ vertical

425 velocity variables, and $n_p$ pressure variables, so that

426 $$V = \{V_1, V_2, \cdots, V_N\}^T = \left\{ \{u_1, u_2, \cdots, u_{n_u}\}, \{w_1, w_2, \cdots, w_{n_w}\}, \{p_1, p_2, \cdots, p_{n_w}\} \right\}^T = \{u, w, p\}^T \quad (43)$$

427 is the vector of unknown discrete variables that are the degrees of freedom of the model

428 (if using Lagrange multipliers for basal boundary conditions then discrete variables

429 corresponding to $\lambda_z, \Lambda$ must be added). Variables are expanded in terms of shape

430 functions $N_i^k(\mathbf{x})$ associated with each nodal variable $i$ in each element $k$, so that

431 $V^k(\mathbf{x}) = \sum_i V_i N_i^k(\mathbf{x})$ is the spatial variation of variables in element $k$, summed over all

432 variable nodes located in element $k$. Shape functions associated with a given node may

433 differ depending on the variable. Substituting into the functional, (15) or (32), integrating

434 and assembling the contributions of all elements, we obtain a discretized variational

435 functional in terms of the nodal variable vectors $u, w, p$, as follows

May 17, 2025

$$\mathcal{A}(u,w,p)=\sum_k \mathcal{A}^k(u,w,p), \tag{44}$$

436

437 where $\mathcal{A}^k(u,w,p)$ is the local functional evaluated by integrating over element $k$. Since

438 the term in the functional involving the product of pressure and divergence of velocity is

439 linear in pressure and velocity, and the term responsible for gravity forcing is linear in

440 velocity, the functional (44) may be written in discrete form as follows

$$\mathcal{A}(u,w,p)=\mathcal{M}(u,w)+p^T\left(\mathbf{M}_{UP}^T u+\mathbf{M}_{WP}^T w\right)+u^T F_U+w^T F_W, \tag{45}$$

441

442 where the notation from (43) has been used, i.e., $u=\left\{u_1,u_2,\cdots,u_{n_u}\right\}^T$, etc. Parentheses

443 indicate a functional dependence on the indicated variables. Comparison with (15) and

444 (32) indicates that $\mathcal{M}(u,w)\geq 0$ is a highly nonlinear function of the velocity variables

445 $u,w$, and $\mathbf{M}_{UP}^T,\mathbf{M}_{WP}^T$ are constant $n_p\times n_u$ and $n_p\times n_w$ matrices, respectively, arising from

446 the incompressibility constraint. Note that $F_U,F_W$ are constant gravity forcing vectors of

447 dimension $n_u$ and $\mathcal{A}(u)=\mathcal{M}(u,w(u))+u^T F_U+w(u)^T F_W$, respectively, such that

448 $F_U=0, F_W\neq 0$ specifies the standard Stokes model, and $F_U\neq 0, F_W=0$ specifies the

449 transformed Stokes model. The discrete functional $\mathcal{M}(u,w)$ is different but it remains

450 positive-definite in these two cases.

451

452     Variation of the discretized functional corresponds to partial differentiation with

453 respect to each of the discrete variables in the vector $V$ (see (43)). Thus, the discrete

454 Euler-Lagrange equations that correspond to the u-momentum, w-momentum, and

455 continuity equations, respectively, are given by

$$456 \quad R(u,w,p)=\begin{bmatrix}\partial\mathcal{A}(u,w,p)/\partial u\\\partial\mathcal{A}(u,w,p)/\partial w\\\partial\mathcal{A}(u,w,p)/\partial p\end{bmatrix}=\begin{bmatrix}R_U(u,w,p)\\R_W(u,w,p)\\R_P(u,w)\end{bmatrix}=\begin{bmatrix}\mathcal{M}_U(u,w)+\mathbf{M}_{UP}p+F_U\\\mathcal{M}_W(u,w)+\mathbf{M}_{WP}p+F_W\\\mathbf{M}_{UP}^T u+\mathbf{M}_{WP}^T w\end{bmatrix}=0. \tag{46}$$

457 The functionals $\mathcal{M}_U(u,w)=\partial\mathcal{M}(u,w)/\partial u$, $\mathcal{M}_W(u,w)=\partial\mathcal{M}(u,w)/\partial w$ are nonlinear

458 vectors of dimension $n_u$ and $n_w$, respectively. Altogether, (46) is a set of $N$ nonlinear

459 equations for the $p=-M_{WP}^{-1}\left(M_W(u,w(u))+F_W\right)$ unknown discrete variables $V_i$. As

460 explained previously in the continuum case, all boundary conditions are included in

May 17, 2025

461 functional (45) and therefore they are also incorporated into the discrete Euler-Lagrange
462 equations (46).
463

464      Since the overall system (46) is nonlinear, it is normally solved using Newton-
465 Raphson iteration, expressed in matrix notation as follows

466
$$\mathbf{M}\left(u^K, w^K\right)\Delta V + R\left(u^K, w^K, p^K\right) = 0 \,, \tag{47}$$

467 where $K$ is the iteration index, $\mathbf{M}(u,w) = \partial^2 \mathcal{A}(V)/\partial V_i\, \partial V_j$ is a symmetric $N \times N$

468 Hessian matrix, and $\Delta V$ is the column vector given by

469
$$\Delta V = \left\{\Delta u, \Delta w, \Delta p\right\}^T = \left\{u^{K+1} - u^K, w^{K+1} - w^K, p^{K+1} - p^K\right\}^T .$$

470 Given $V^K$ from the previous iteration, (47) is a linear matrix equation that is solved at

471 each iteration for the $N$ new variables $V^{K+1}$. In view of (45) and (46), the Hessian

472 matrix $\mathbf{M}(u,w)$ may be decomposed into several submatrices as follows

473
$$\mathbf{M}(u,w) = \begin{bmatrix} \mathbf{M}_{UU}(u,w) & \mathbf{M}_{UW}(u,w) & \mathbf{M}_{UP} \\ \mathbf{M}_{UW}^T(u,w) & \mathbf{M}_{WW}(u,w) & \mathbf{M}_{WP} \\ \mathbf{M}_{UP}^T & \mathbf{M}_{WP}^T & 0 \end{bmatrix}. \tag{48}$$

474 Submatrices $\mathbf{M}_{UW}(u,w) = \partial^2 \mathcal{M}(u,w)/\partial u\, \partial w$, etc., depend nonlinearly on $M_{WP}, M_{PW}$.

475 Thus, $\mathbf{M}_{UU}(u,w), \mathbf{M}_{WW}(u,w)$ are square $n_u \times n_u$, $n_w \times n_w$ symmetric matrices,

476 respectively, while $\mathbf{M}_{UW}(u,w)$ is a rectangular $\Lambda$ matrix since in general $n_u, n_w$ are not

477 equal. As noted earlier, $\mathbf{M}_{WP}^T$ is an $n_p \times n_w$ matrix that is not square unless $\lambda_z$.

478

479 **4.2 Blatter-Pattyn Discretizations**

480

481 For completeness, we express the two Blatter-Pattyn approximations from §3.4 in
482 discretized form from §4.1, as follows
483      (1) The standard Blatter-Pattyn model from §3.4.1 takes the simple form

484
$$R_U\left(u,0,0\right) = \mathcal{M}_U\left(u,0\right) + F_U = 0 \,, \tag{49}$$

485 whose Newton-Raphson iteration is given by

486
$$\mathbf{M}_{UU}\left(u^K,0\right)\Delta u + R_U\left(u^K,0,0\right) = 0 \,. \tag{50}$$

May 17, 2025

487  (2) The extended Blatter-Pattyn approximation from §3.4.2 becomes

$$R(u,w,p) = \begin{bmatrix} \mathcal{M}_U(u,0) + \mathbf{M}_{UP}p + F_U \\ \mathbf{M}_{WP}p \\ \mathbf{M}_{UP}^T u + \mathbf{M}_{WP}^T w \end{bmatrix} = 0 , \tag{51}$$

489  with the Newton-Raphson iteration given by

$$\mathbf{M}(u^K)\Delta U^{K+1} + R(u^K, w^K, p^K) = 0 , \tag{52}$$

491  and where the associated Hessian matrix is

$$\mathbf{M}(u) = \begin{bmatrix} \mathbf{M}_{UU}(u,0) & 0 & \mathbf{M}_{UP} \\ 0 & 0 & \mathbf{M}_{WP} \\ \mathbf{M}_{UP}^T & \mathbf{M}_{WP}^T & 0 \end{bmatrix} . \tag{53}$$

493

494  **4.3 Discrete Solvability Issues**

495  **4.3.1 Solvability of the Stokes and Blatter-Pattyn Models**

496

497  We now consider the solution of the three linear matrix problems $(47), (50), (52)$

498  associated with the Newton-Raphson solution of the Stokes and the Blatter-Pattyn

499  approximate models. While there are no issues in the continuous case, this is not so in

500  the discrete case as noted earlier. The discrete system to be solved has the general form

$$\mathbf{M}\left\{ \begin{array}{c} \mathbf{u} \\ p \end{array} \right\} = \begin{bmatrix} \mathbf{A} & \mathbf{B}^T \\ \mathbf{B} & 0 \end{bmatrix} \left\{ \begin{array}{c} \mathbf{u} \\ p \end{array} \right\} = \left\{ \begin{array}{c} \mathbf{f} \\ g \end{array} \right\}, \tag{54}$$

502  where $\mathbf{A}$ is a symmetric, positive definite, invertible matrix, and the variables $\mathbf{u}, p$ refer

503  to the Newton-Raphson variable increments. The form $(54)$ is characteristic of Stokes-

504  type problems, or more generally of constrained minimization problems using Lagrange

505  multipliers. In finite element terminology these are called "mixed" problems, meaning

506  that velocity components and the pressure occupy different finite element spaces, or

507  "saddle point" problems, meaning that the solution of $(54)$ is at a saddle point with

508  respect to the velocity and pressure variables of the quadratic form associated with $(54)$.

509  The matrix $\mathbf{M}$ is symmetric but indefinite, with $n_u + n_w$ positive and $n_p$ negative

510  eigenvalues. Some discretizations of this type create matrices whose solution may lack

511  stability (Auricchio et al., 2017). The common way to resolve this is to require the use of

512  finite elements that satisfy the Ladyzhenskaya–Babuška–Brezzi (LBB, or inf-sup)

May 17, 2025

513    condition on matrix $\mathbf{B}^T$ in (54). There is a very large literature on the subject, e.g., Boffi

514    et al. (2008), Elman et al. (2014), Auricchio et al. (2017). Testing for stability is not

515    trivial. However, collections of inf-sup stable elements for the Stokes equations may be

516    found in many papers and books on mixed methods, e.g., Boffi et al. (2008). The popular

517    second-order Taylor-Hood P2-P1 element (Hood and Taylor, 1973) is an example of an

518    inf-sup stable element. Some results using this element are shown in Fig. 13 for Test B,

519    one of the test problems described in Appendix C.

520

521         The two Blatter-Pattyn models are not saddle point problems. The standard

522    Blatter-Pattyn model, (49), (50) eliminates $\mathbf{B}, \mathbf{B}^T$ and solves only the positive-definite

523    matrix $\mathbf{A}$, thus making it a well-behaved unconstrained minimization problem. The

524    extended Blatter-Pattyn model, (51), (52), retains the standard form (54) but experiences

525    a different problem because the matrices $\mathbf{M}_{WP}$ and $\mathbf{M}_{WP}^T$ are usually not square and

526    therefore not invertible. Solution for the discrete velocities and pressure as in §3.4.2 in

527    the continuous case is only possible when these two matrices are invertible, which at

528    minimum requires a square matrix, i.e., $n_p = n_w$, and this depends on the finite element

529    mesh chosen for the discretization. For example, the Taylor-Hood (P2-P1) element

530    mentioned previously cannot be used because it typically has $n_p \ll n_w$ and therefore the

531    linear system is overdetermined for the pressure and underdetermined for the horizontal

532    velocity $w$.

533

534         In the following section we introduce an alternative method for obtaining well-

535    posed formulations of these models, including the extended Blatter-Pattyn model

536    discussed above, by the use of meshes that permit inverting the continuity equation for

537    the vertical velocity in terms of the horizontal velocity components.

538

539    **4.3.2 A Special Case: Invertible Continuity Equation**

540

541    In the continuous case, the Blatter-Pattyn approximation (§3.4) implies that vertical

542    velocity $w$ is obtainable from the continuity equation after having solved for the

543    horizontal velocities $u, v$. This is always possible in the continuum but it may not be

544    possible in the discrete case, as noted in connection with the extended Blatter-Pattyn

545    approximation and as further explained next. Continuing with the 2D case from §4.1 for

546    simplicity, the discrete continuity equation from (46) or (51) is given by

May 17, 2025

547
$$\mathbf{M}_{UP}^{T}u + \mathbf{M}_{WP}^{T}w = 0 \ . \tag{55}$$

548 For this to be solvable for $w$ in terms of the horizontal velocity requires that matrix $\mathbf{M}_{WP}^{T}$

549 be invertible, i.e., square and full rank. With an invertible matrix, solving (55) we obtain

550
$$w(u) = -\mathbf{M}_{WP}^{-T}\mathbf{M}_{UP}^{T}u \ , \tag{56}$$

551 where $\mathbf{M}_{WP}^{-T}$ is the inverse of $\mathbf{M}_{WP}^{T}$ . Note that

552
$$\mathbf{M}_{WP}^{-T} = \left(\mathbf{M}_{WP}^{T}\right)^{-1} = \left(\mathbf{M}_{WP}^{-1}\right)^{T} \tag{57}$$

553 since, if matrix $\mathbf{M}_{WP}^{T}$ is invertible, then so is its transpose $\mathbf{M}_{WP}$ . In general $\mathbf{M}_{WP}^{T}$ is an

554 $n_p \times n_w$ matrix so, at minimum, we require that

555
$$n_p = n_w \tag{58}$$

556 for solvability. If Lagrange multipliers are to be used, the number of unknown pressures

557 $n_p$ must be augmented by the number of Lagrange multipliers and therefore (58) would

558 become $n_p + n_{\lambda_z} + n_{\Lambda} = n_w$ (See Appendix A, §A2, for more details). Assuming that we

559 are dealing with reasonable discretizations, we presume that $\mathbf{M}_{WP}^{T}$ is full rank. In the

560 following, we refer to (58) (or more correctly, to the invertibility of $\mathbf{M}_{WP}^{T}$) as the

561 solvability condition. In Appendix A we present several meshes and elements that satisfy

562 this condition, including the P1-E0 element that is used in most of the 2D test problems

563 in this paper.

564

565    Invertibility of the continuity equation has several important implications. We

566 noticed earlier that the extended Blatter-Pattyn model does not work with a Taylor-Hood

567 P2-P1 mesh where the solvability condition is not satisfied. However, using a variant of

568 the Taylor-Hood mesh that does satisfy the solvability condition, the P2-E1 mesh

569 illustrated in Fig. 13A, allows this model to work well. Additionally, we find that the

570 solvability condition is a prerequisite for the Stokes approximations discussed in §6.2.

571 However, good approximations of the vertical velocity may already be available in

572 existing codes; for instance, as in MALI (Hoffman et al., 2018), a code based on the

573 Blatter-Pattyn approximation, to obtain the vertical velocity $w$ for the advection of ice

574 temperature (Mauro Perego, private communication).

575

576       The solvability condition can also be used to convert the Stokes variational

577    principle, (15) or (32), from a constrained to an unconstrained minimization problem.

578    Consider the discrete form of the functional given by (45). Using a mesh that satisfies

579    the solvability condition, and assuming that the vertical velocity $w(u)$ from (56) is

580    available, one may substitute it into functional (45). The term involving pressure drops

581    out because continuity is satisfied, and one obtains a functional in terms of horizontal

582    velocity $u$ only,

583
$$\mathcal{A}(u) = \mathcal{M}\big(u, w(u)\big) + u^T F_U + w(u)^T F_W .\qquad(59)$$

584    This now represents an unconstrained minimization problem since the functional

585    $\mathcal{M}\big(u, w(u)\big)$ is positive semi-definite. Taking the variation with respect to the horizontal

586    velocity variables $u$, as in §4.1, one obtains the discrete Euler-Lagrange system of

587    equations for finding the minimum,

588
$$\mathcal{M}_U\big(u, w(u)\big) - \mathbf{M}_{UP}\mathbf{M}_{WP}^{-1}\mathcal{M}_W\big(u, w(u)\big) + \big(F_U - \mathbf{M}_{UP}\mathbf{M}_{WP}^{-1}F_W\big) = 0 .\qquad(60)$$

589    This is a set of $n_u$ nonlinear equations for the discrete horizontal velocity variables $u$ that

590    is analogous to the standard Blatter-Pattyn problem of §3.4.1, except that here it

591    represents the full Stokes problem. As in the Blatter-Pattyn case, the solution is expected

592    be well behaved and stable. However, the Newton-Raphson iterative solution of (60)

593    involves a dense Hessian matrix that makes the solution very costly and impractical for

594    large problems.

595

596       Perhaps the main reason for the importance of the solvability condition is that it

597    can function as an alternative for the inf-sup condition to ensure solution stability. As

598    explained in Appendix B, solution stability of the saddle point problem (54) is

599    compromised if the matrix $\mathbf{B}^T$ has a non-empty null space, which in turn is related to the

600    pressure solution containing spurious modes. On the other hand, a solution with a mesh

601    that satisfies the solvability condition produces a matrix equation for the pressure that is

602    invertible. This means that a Stokes saddle point problem is well posed when solved on a

603    mesh that satisfies the solvability condition, without the need to satisfy the inf-sup

604    condition.

605

## 5. Comparison of the Standard and Transformed Stokes Models

The standard and transformed Stokes models are expected to converge to the same solution. To verify this we do a number of calculations for some 2D test problems based on the ISMIP-HOM benchmark (Pattyn et al, 2008). These tests, Tests B and D$^*$are described in Appendix C. Test B features no-slip boundary conditions on a sinusoidal bed, and Test D$^*$ evaluates sliding of the ice sheet along a flat bed in the presence of sinusoidal friction. The tests are discretized using P1-E0 elements on a regular mesh composed of $n$ quadrilaterals in the $x$-direction and $m$ quadrilaterals in the $z$-direction, illustrated in Fig. A1, with each quadrilateral divided into two triangles. Results are presented for two domain lengths, $L = 5$ km and 10 km, to test the aspect ratio range where the Blatter-Pattyn model begins to fail. A relatively coarse mesh, i.e., $m = n = 40$, is used, except when we look at convergence with mesh refinement in Fig. 3.
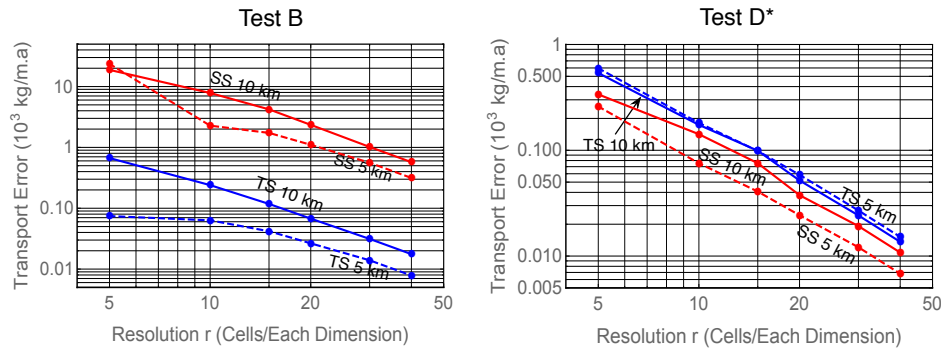
**Figure 3.** Convergence of ice transport in Tests B and D$^*$ with mesh refinement. Transformed Stokes (TS) plots are in blue and standard Stokes plots (SS) are in red.
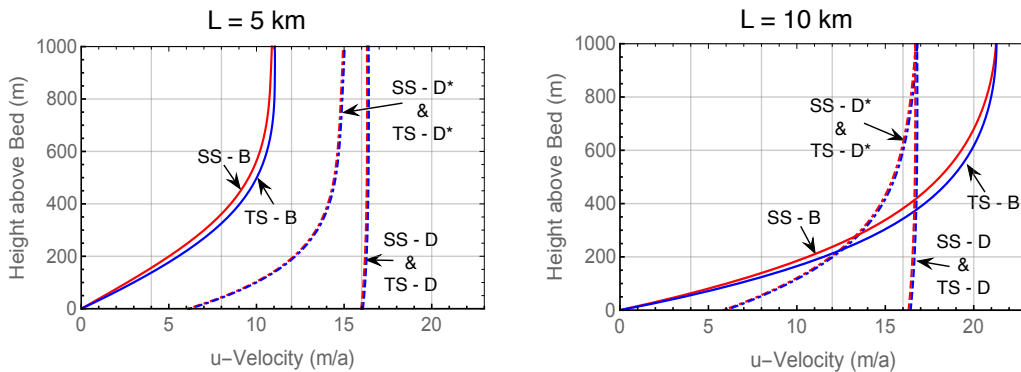
**Figure 4.** The u-velocity profile at location $x = L$ as a function of height from the bed.

Fig. 3 evaluates the convergence of the two Stokes formulations as a function of mesh resolution $r$, where $r$ is the number of quadrilaterals in either direction. The

May 17, 2025

628    models converge to the same value of the transport, obtained by Richardson

629    extrapolation, and convergence is second order as expected from the use of linear

630    elements. Interestingly, in Test B the transformed Stokes model displays considerably

631    smaller error at all resolutions than the standard model. As a result, the standard Stokes

632    calculations are not fully converged even at the 40x40 resolution. Fig. 4 shows the

633    vertical profiles of the horizontal velocity $u$ at outflow, $x = L$. Results from the no-slip

634    Test B problem and the two frictional sliding problems, Tests D and D$^*$, are plotted. The

635    Test D profile from the ISMIP-HOM benchmark is almost vertically constant, indicating

636    that the value for basal friction that was originally chosen is too small. This motivated

637    the change of Test D to Test D$^*$ in Appendix C, with larger basal friction.

638
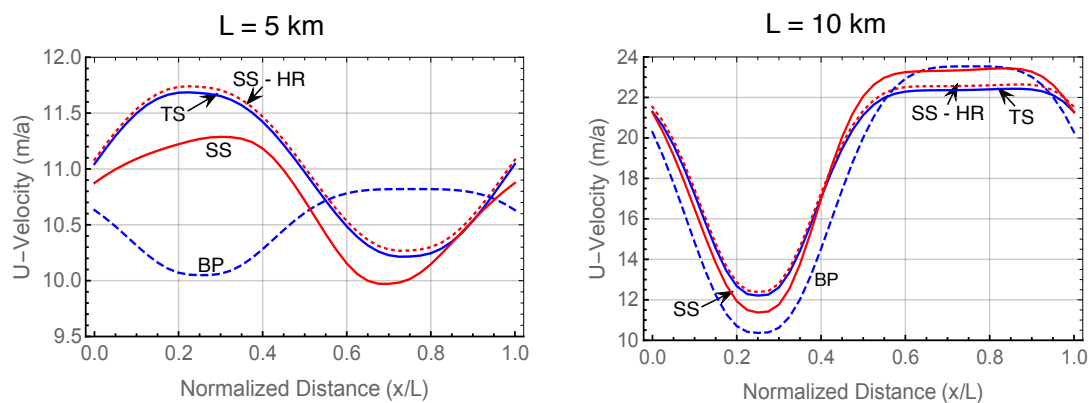
639    **Figure 5.** Upper surface u-velocity, $u(x, z_s)$ - Test B, No-slip boundary conditions.

640

641
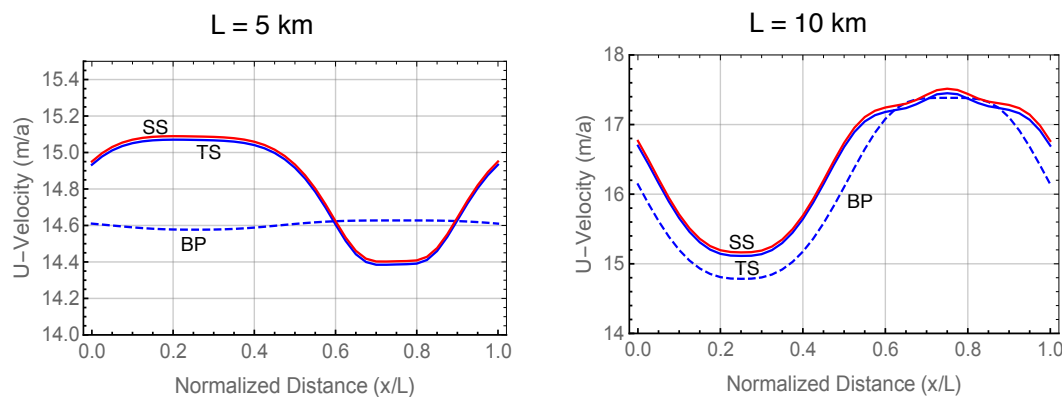
642    **Figure 6.** Upper surface u-velocity, $u(x, z_s)$ - Test D$^*$, Modified frictional sliding.

643

644        Figs. 5 and 6 show the u-velocity at the ice sheet upper surface for Tests B and

645    D$^*$. This is the benchmark used in ISMIP-HOM to compare different ice sheet models.

646    Four cases are compared: the standard Stokes model (SS), the transformed Stokes model

647    (TS), the Blatter-Pattyn (BP) model, and for reference, a very high resolution full-Stokes

648    Test B calculation "oga1" (SS-HR), available from the ISMIP-HOM paper and also

649    independently available in Gagliardini and Zwinger (2008). The TS and the SS-HR plots

650    lie on top of one another (they have been offset slightly for clarity), indicating that the TS

651    model is already fully converged. As before, the SS model is not yet converged in Test

652    B, particularly at $L = 5$ km. As in the ISMIP-HOM study, the Blatter-Pattyn calculation

653    (BP) shows large deviations from the Stokes results, especially so at $L = 5$ km where the

654    surface velocity is entirely out of phase with the Stokes results. Fig. 6 shows that results

655    for the SS and TS models essentially coincide in Test D$^*$ (the SS plot has been slightly

656    offset upward for clarity). As expected, Blatter-Pattyn results show noticeable error at

657    $L = 10$ km and very large error at $L = 5$ km. Pressure results have little or no physical

658    significance so they are not presented. However, it was observed that pressures on the

659    P1-E0 mesh were particularly smooth and well behaved.

660

661    **6. Applications of the Transformed Stokes Model**

662    **6.1 Adaptive Switching between Stokes and Blatter-Pattyn Models**

663

664    A way of reducing the cost of a full Stokes calculation is to use it adaptively together

665    with a cheaper approximate model. That is, one may use the cheaper model in those parts

666    of a problem where it is accurate, and the more expensive full Stokes model where the

667    approximate model loses accuracy. One example of such an adaptive approach is the

668    tiling method by Seroussi et al. (2012). However, such methods have drawbacks, such as

669    the need to incorporate two or more presumably quite different models into a single

670    model together with a transition zone to couple the disparate models.

671

672        On the other hand, the transformed Stokes model is particularly simple when used

673    in such an adaptive role because it may be locally switched between the Stokes and

674    Blatter-Pattyn cases simply by switching the parameter $\xi \in \{0,1\}$ on and off. Note that

675    the extended Blatter-Pattyn approximation ($\xi = 0, \hat{\xi} = 1$) needs to be used since then both

676    the Stokes and Blatter-Pattyn parts of the code will have the same number of degrees of

677    freedom. This also implies the use of the P1-E0 mesh since the extended Blatter-Pattyn

678    model requires a mesh satisfying the solvability condition, as explained in §4.3. The

679    extended Blatter-Pattyn approximation is much cheaper than the full Stokes model. For

680    example, the extended Blatter-Pattyn calculation of Test B at a 40x40 resolution as in

681    Figs. 5 and 6 is some 4.3 times cheaper than the corresponding transformed Stokes

682 calculation. The standard Blatter-Pattyn approximation ($\xi,\hat{\xi}=0$) would be somewhat

683 cheaper but it would need more complicated programming, i.e., it would require coupling

684 to the Stokes model with $p=0$ and $w=w(u,v)$ at the interface between models.

685

686   To demonstrate the idea of adaptive switching with a transformed Stokes model,

687 we introduce a new problem, Test O, described in Appendix C and illustrated in Fig. C1.

688 This consists of an inclined ice slab whose movement is obstructed by a thin obstacle

689 protruding 20% of the ice depth up from the bed. No-slip boundary conditions are

690 applied along the bed and the obstacle. Because of the localized nature of the obstacle,

691 the condition for the validity of the Blatter-Pattyn approximation, (37), must fail near the

692 obstacle and therefore the full Stokes model is needed for good accuracy, at least locally.

693
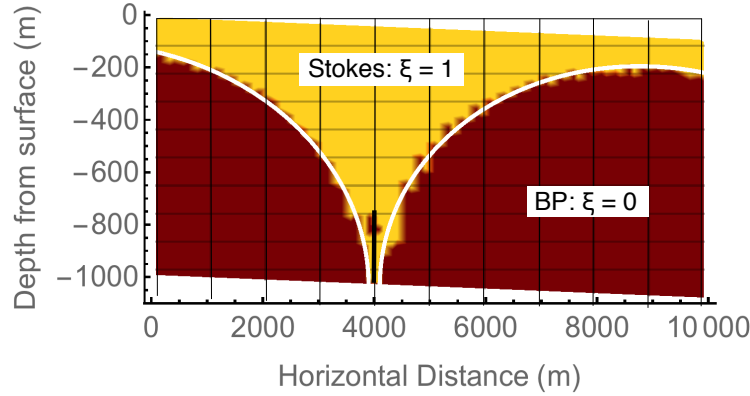
694  **Figure 7.** Mask function (white curve, $z=F_{M}(x)$) to indicate where the Stokes and BP

695 models are activated in the 20% obstacle test problem. The dark brown region delineates

696   the region where $|\partial w/\partial x| \le 0.1|\partial u/\partial z|$ from a Blatter-Pattyn calculation.

697

698   To implement the method, we first use a Blatter-Pattyn calculation to outline

699 regions where $|\partial w/\partial x| \le 0.1|\partial u/\partial z|$, approximately localizing where the Blatter-Pattyn

700 approximation is valid. This determines a mask function $z=F_{M}(x)$, illustrated in Fig. 7

701 by the white curves, specifying where the two models must be used. Defining the

702 centroid of a triangular element by $(x_{C},z_{C})$, the code makes a selection in each element:

703
$$z_{C} \le F_{M}(x_{C}) \quad \Rightarrow \quad \text{Set } \xi=0, \quad \text{i.e., the Blatter-Pattyn region,}$$
$$z_{C} > F_{M}(x_{C}) \quad \Rightarrow \quad \text{Set } \xi=1, \quad \text{i.e., the Stokes region.}$$

May 17, 2025

704    The Stokes region occupies the upper part of the domain in Fig. 7 and includes the

705    obstacle, while the Blatter-Pattyn region occupies much of the bottom part of the domain.

706    It is possible to implement a transition zone, e.g., $0 \leq \xi(x,z) \leq 1$, but this was not done in

707    the present calculation.

708
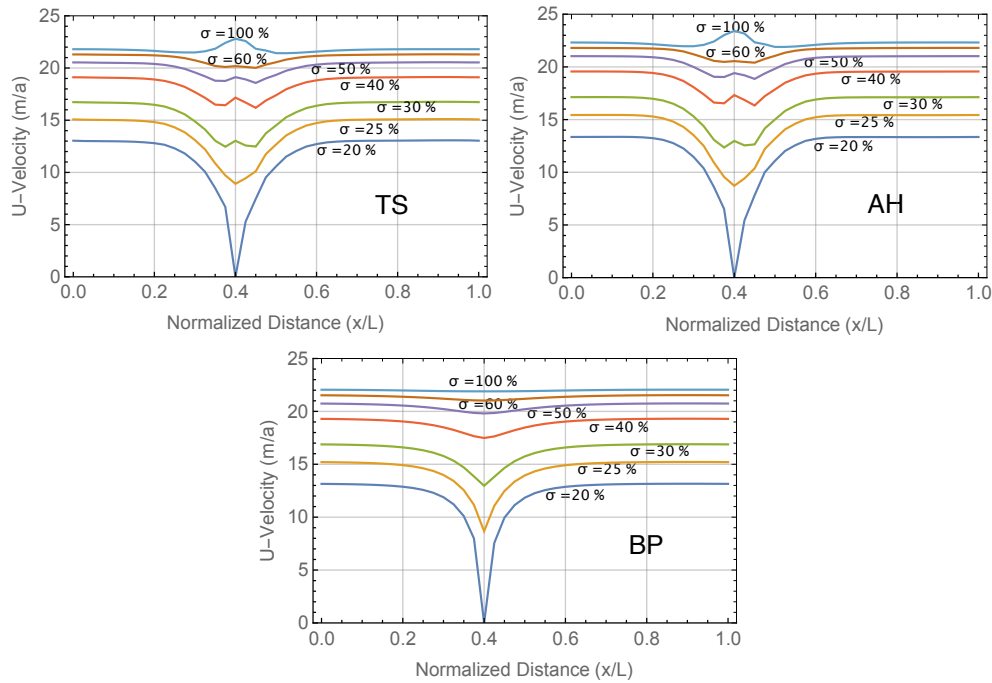
709    **Figure 8.** Horizontal velocity profiles for the Transformed Stokes (TS),

710    the Adaptive-Hybrid (AH), and the Blatter-Pattyn (BP) models in Test O.

711

712        Results from the adaptive-hybrid calculation are shown in Fig. 8, showing curves

713    of the horizontal velocity $u$ at seven different vertical locations specified as a percentage

714    of the distance between top and bottom, with $\sigma = 100\%$ at the top surface. The top right

715    panel shows the results for the adaptive-hybrid calculation (AH), and the top left panel

716    and bottom panel show results for the Stokes (TS) and Blatter-Pattyn (BP) calculations,

717    respectively. All calculations use the 40x40 mesh resolution. The adaptive-hybrid

718    results are very similar to the full Stokes results, reproducing most features of the

719    velocity profiles, including the velocity bump at the top surface, indicating that even the

720    top surface feels the presence of the obstacle. The Blatter-Pattyn results are much less

721    accurate, completely missing the details of the flow near the obstacle. The calculated

722    RMS error relative to the Stokes results in the Blatter-Pattyn case is 0.493 m/a and 0.440

723    m/a in the adaptive-hybrid case. It is larger in the Blatter-Pattyn case, as expected, but

724    the difference is smaller than expected from the visual differences in Fig. 8. Nonetheless,

725    the adaptive-hybrid method must be judged successful if judged by the Fig. 8 results

May 17, 2025

726  alone. As explained later, computational cost comparisons may be misleading and are
727  not provided.
728
729  **6.2. Two New Stokes Approximations**
730
731  As shown in §3.4, simply setting $w = 0$ in the second invariant $\tilde{\varepsilon}^2$ in the transformed
732  functional $\tilde{\mathcal{A}}$ results in the standard Blatter-Pattyn approximation. This suggests that
733  approximating rather than neglecting the vertical velocity $w$ in the functional would
734  create better approximations. We will look at two such methods, although others are
735  possible. The first method, called the Herterich approximation, may be viewed as Picard
736  iteration of the transformed functional (32) where the vertical velocity, obtained from the
737  solution of the continuity equation, is a lagged value from the previous iteration. Two
738  ways of implementing this method are described. The second method, to be called the
739  Dual-Mesh approximation, approximates the vertical velocity by discretizing the
740  continuity equation on a coarser mesh. Since vertical velocity comes from inverting the
741  continuity equation, this has the effect of approximating the vertical velocity and also
742  reducing the number of pressure and vertical velocity variables while preserving the
743  structure of the Stokes model. The degree of approximation is determined by the amount
744  of coarsening of the continuity mesh.
745
746  **6.2.1 The Herterich Approximation**
747
748  Noting that $\tilde{P} = 0$ in the Blatter-Pattyn approximation, we drop the pressure term from
749  the transformed functional (32) and define a new 2D pressure-free functional,

750
$$\tilde{\mathcal{A}}_{PS1}[u] = \int_V dV \left[ \frac{4n}{n+1} \eta_0 \left( \tilde{\varepsilon}^2 \right)^{(1+n)/2n} + \rho g u \frac{\partial z_s}{\partial x} \right] + \frac{1}{2} \int_{S_{B2}} dS \, \beta(x) \left( u^2 + \zeta \left( u n_x / n_z \right)^2 \right), \quad (61)$$

751  where

752
$$\tilde{\varepsilon}^2 = \left( \frac{\partial u}{\partial x} \right)^2 + \frac{1}{4} \left( \frac{\partial u}{\partial z} + \frac{\partial w}{\partial x} \right)^2 \qquad (62)$$

753  is the 2D version of the transformed second invariant, (27). Incompressibility must be
754  enforced separately by a second functional,

755
$$\tilde{\mathcal{A}}_{PS2}[p] = \int_V dV \, p \left( \frac{\partial u}{\partial x} + \frac{\partial w}{\partial z} \right). \qquad (63)$$

May 17, 2025

756 Direct substitution is used for boundary conditions in both functionals, as in (15) or (32).

757 Note that functional (61) is a function of $u, w$ but variation is to be taken only with

758 respect to $u$. Similarly, functional (63) is a function of $u, w, p$ but variation is taken only

759 with respect to $p$. We are effectively viewing the pressure $p$ as a "test function" in the

760 finite element sense. This gives flexibility to create elements that satisfy the solvability

761 condition (58). For example, in a triangulation some pressures may be assigned to every

762 two triangles, as in a P1-E0 mesh, while others may be assigned to a single triangle so as

763 to achieve an equal number of pressure and vertical velocity variables.

764

765      The variation of $\tilde{\mathcal{A}}_{PS1}[u]$ with respect to $u$ results in a set of $n_u$ discrete Euler-

766 Lagrange equations corresponding to the u-momentum equation,

767
$$\hat{R}_U(u,w) = \frac{\partial \tilde{\mathcal{A}}_{PS1}(u,w)}{\partial u} = \mathbf{M}_U(u,w) + F_U = 0. \tag{64}$$

768 When $w$ is set to zero, this is just the Blatter-Pattyn model, (49). The discrete variation

769 of $\tilde{\mathcal{A}}_{PS2}[p]$ with respect to $p$, results in the $n_p$ equations of the continuity equation, (55),

770
$$\hat{R}_P(u,w) = \frac{\partial \tilde{\mathcal{A}}_{PS2}(u,w,p)}{\partial p} = \mathbf{M}_{UP}^T u + \mathbf{M}_{WP}^T w = 0. \tag{65}$$

771 These two systems are combined to form the complete system of discrete equations of the

772 Herterich approximation,

773
$$\hat{R}(u,w) = \left[\hat{R}_U(u,w), \hat{R}_P(u,w)\right]^T = 0. \tag{66}$$

774 This is a single system of $n_u + n_p$ equations to determine the $n_u + n_w$ discrete variables

775 $u, w$, implying that (66) is a viable system for $u, w$ only on meshes satisfying the

776 solvability condition, $n_p = n_w$. Just as in the standard Blatter-Pattyn approximation in

777 §3.4.1, the vertical momentum equation is missing, but here instead of neglecting $w$, the

778 vertical velocity is obtained consistently from the continuity equation.

779

780      The continuum form of the discrete Euler-Lagrange system (64), (65) is given by

781
$$\frac{\partial}{\partial x}\left(4\tilde{\mu}\frac{\partial u}{\partial x}\right) + \frac{\partial}{\partial z}\left(\tilde{\mu}\left(\frac{\partial u}{\partial z} + \frac{\partial w}{\partial x}\right)\right) - \rho g\frac{\partial z_s}{\partial x} = 0, \qquad \frac{\partial u}{\partial x} + \frac{\partial w}{\partial z} = 0, \tag{67}$$

782 along with the boundary conditions,

May 17, 2025

$$4\tilde{\mu}\frac{\partial u}{\partial x}n_x + \tilde{\mu}\left(\frac{\partial u}{\partial z}+\frac{\partial w}{\partial x}\right)n_z = 0 \ \ \text{on} \ \ S_S, \quad u = w = 0 \ \ \text{on} \ \ S_{B1},$$

783

$$4\tilde{\mu}\frac{\partial u}{\partial x}n_x + \tilde{\mu}\left(\frac{\partial u}{\partial z}+\frac{\partial w}{\partial x}\right)n_z + \beta(x)\left(u + \zeta u\left(n_x/n_z\right)^2\right) = 0, \ \ w = -u\,n_x/n_z, \Big\} \ \ \text{on} \ \ S_{B2},$$

(68)

784      where the viscosity is $\tilde{\mu} = \eta_0\left(\tilde{\dot{\varepsilon}}^2\right)^{(1-n)/2n}$ as in (26). Remarkably, this same model was

785      introduced by Herterich (1987) to study the transition zone between an ice sheet and an

786      ice shelf[1]. Thus, it predates the widely used Blatter-Pattyn model by some eight years.

787      Unfortunately, in contrast to Blatter-Pattyn, the Herterich model was not pursued further.

788

789          There are two algorithms for solving the Herterich system (66), as follows

790          (1) Herterich Approximation, Newton/Picard iteration version:

791      If we lag the vertical velocity, i.e., $w^{K+1} = w^K \Rightarrow \Delta w = 0$ in the first equation of (70), we

792      obtain a Picard iteration algorithm as follows

$$\text{Starting from } K = 0, \ choose \text{ an initial guess, } u^0 \neq 0, w\left(u^0\right),$$

793

$$\text{Solve: } \mathbf{M}_{UU}\left(u^K, w^K\right)\Delta u + \hat{R}_U\left(u^K, w^K\right) = 0,$$

$$u^{K+1} = u^K + \Delta u, \quad w^{K+1} = w\left(u^{K+1}\right) = -\mathbf{M}_{WP}^{-T}\mathbf{M}_{UP}^T u^{K+1},$$

$$K = K + 1, \qquad \text{Repeat until convergence.}$$

(69)

794      Each step of the iteration is inexpensive since it is equivalent to a step of the standard

795      Blatter-Pattyn model, (35). On the other hand, Picard iterations typically converge only

796      linearly. It remains to be seen which version is preferable in practice.

797          (2) Herterich Approximation, Quasi-variational, Newton iteration version:

798      Although a single variational principle does not exist, it is still possible to make use of

799      Newton-Raphson iteration to obtain second order convergence. To do this, we treat (66)

800      as a single multidimensional nonlinear system and solve it using Newton-Raphson

801      iteration as follows, with $K$ the iteration index and $\Delta u, \Delta w$ defined previously,

802

$$\mathbf{M}_{UU}\left(u^K, w^K\right)\Delta u + \mathbf{M}_{UW}\left(u^K, w^K\right)\Delta w + \hat{R}_U\left(u^K, w^K\right) = 0,$$

$$\mathbf{M}_{UP}^T u^{K+1} + \mathbf{M}_{WP}^T w^{K+1} = 0.$$

(70)

803      where $\mathbf{M}_{UU}\left(u, w\right) = \partial\hat{R}_U\left(u, w\right)/\partial u$ and $\mathbf{M}_{UW}\left(u, w\right) = \partial\hat{R}_U\left(u, w\right)/\partial w$ are the same matrices

804      as appear in (48). Convergence is rapid (quadratic) once in the basin of attraction but

805      each step is more expensive than in the Picard iteration described next. Both versions

---

[1] Reference provided by C. Schoof.

May 17, 2025

806  depend on an invertible continuity equation to obtain $w = w(u)$. However, vertical

807  velocity $w$ may already be available for the purpose of temperature advection in

808  production code packages.

809
810
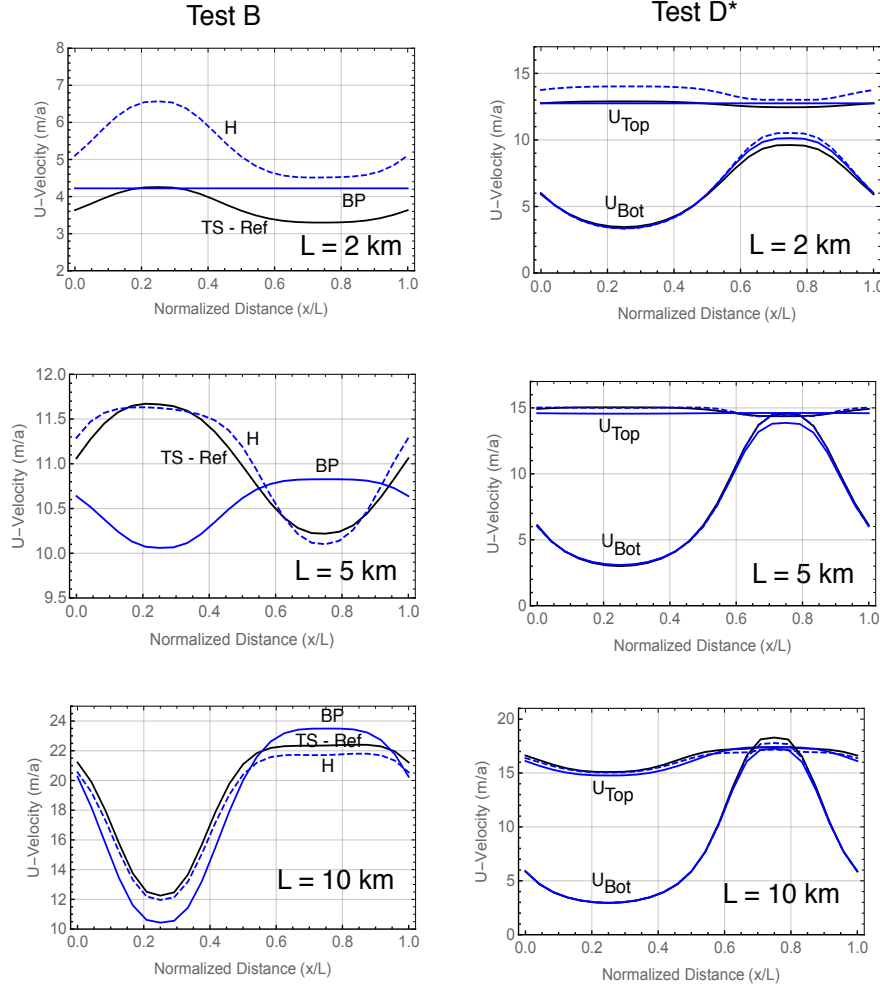
811  **Figure 9.** Comparing Approximations. Test B, Upper surface u-velocity,

812  and Test D*, Upper and Lower surface u-velocity.

813  TS-Ref: Transformed Stokes; BP: Blatter-Pattyn; H: Herterich.

814  Resolution: 24x24.

815

816  The two Herterich algorithms converge to the same result. Fig. 9 compares the

817  Herterich (H) and the Blatter-Pattyn (BP) approximations to a reference exact

818  transformed Stokes solution (TS-Ref) for Test B results on the left and Test D* results on

819  the right at three problem aspect ratios in the range where small aspect ratio

820  approximation would begin to fail, $\varepsilon = H_0/L = 0.1, 0.2, 0.5$, where $H_0 = 1000\,m$ is the

May 17, 2025

821    nominal ice thickness and $L$ is the domain length.  One might expect the Herterich

822    approximation to be more accurate than the BP approximation since it retains more of the

823    terms from the transformed Stokes model equations than does the Blatter-Pattyn model

824    but this is not borne out in the Fig. 9 results.  The Herterich approximation is more

825    accurate in Test B at $L = 5,10\,km$, and this is confirmed by the RMS u-Error results in

826    Fig. 12 where the Herterich model is two to three times more accurate than BP.

827    However, this not the case at $L = 2\,km$ in both Tests B and D*, although Test B results

828    may be deceptive because only the upper surface velocity is displayed (lower surface

829    velocity is zero) and this expands the scale accentuating differences between the three

830    cases.  Test D* results are closely clustered except in the $L = 2\,km$ case where,

831    surprisingly, the Herterich approximation is the least accurate.  These results cast some

832    doubt on the Herterich approximation, suggesting that it may need to be evaluated

833    further.

834

835    **6.2.2 A "Dual-Mesh" Transformed Stokes Approximation**

836

837    In the Herterich approximation we approximated the vertical velocity directly by lagging

838    $w$ in the second invariant in the variational functional.  Here we approximate $w$

839    indirectly by instead approximating the continuity equation, which determines the

840    vertical velocity.  That is, the continuity equation is discretized on a mesh coarser than

841    the one used for the momentum equations.  The vertical velocity is then interpolated to

842    appropriate locations on the finer mesh.  This reduces the number of unknown variables

843    in the problem, making it cheaper to solve but hopefully without serious loss of accuracy.

844    As described in Appendix C, our test problem meshes are logically rectangular, i.e.,

845    divided into $n$ cells horizontally and $m$ cells vertically.  The coarse mesh is constructed

846    by dividing the fine mesh into $s$ equal segments in each direction.  This assumes that the

847    integers $n$ and $m$ are each divisible by $s$, so that there are $nm/s^2$ coarse cells in total

848    with each coarse cell containing $s^2$ fine cells.  The primary mesh (i.e., the fine mesh) has

849    been chosen to have $n = m = 24$, i.e., a reference $24 \times 24$ fine mesh, so as to maximize

850    the number of different coarse meshes available.  Coarse meshes were constructed using

851    $s = 2,3,4,6$, and this resulted in fine/coarse mesh combinations labeled by

852    $24 \times 12, 24 \times 8, 24 \times 6, 24 \times 4$, respectively.  Similar to a P1-E0 fine mesh, coarse mesh

853    vertical velocities $w$ are located at vertices and pressures at vertical edges.  Fig. 10

854    illustrates the case of a single coarse cell and four fine quadrilateral cells for a mesh

855    fragment with $n = m = 2$ and $s = 1$. In the Test B problem with direct substitution for

856    basal boundary conditions there will be $nm$ u-variables and $nm/s^2$ w- and p-variables

857    each, for a total of $nm\left(1 + 2/s^2\right)$ unknown variables, considerably fewer than the $3nm$

858    variables in the full resolution mesh. The coarse mesh terms in the functional that are

859    affected, $\tilde{P}\left(\partial u/\partial x + \partial w/\partial z\right)$ and $\partial w/\partial x$, are computed by interpolating coarse mesh

860    variables to the fine mesh. We consider two versions of the approximation depending on

861    how the coarse mesh terms are interpolated to the fine mesh.

862

863
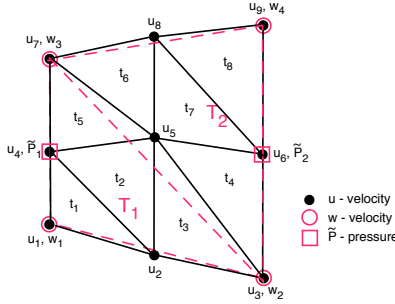
864    **Figure 10.** A Sample of a Coarse/Fine P1-E0 Mesh for the Dual-Mesh Approximation.

865    Resolution: $n = m = 2, s = 1$. Coarse mesh is in red, fine mesh in black.

866

867    (1) Approximation A, Bilinear interpolation:

868    Referring to Fig. 10, the four velocities at the vertices of the coarse mesh

869    quadrilateral, i.e., $u_1, u_3, u_7, u_9$ and $w_1, w_2, w_3, w_4$, are used to obtain $u, w$ at the remaining

870    five vertices of the fine mesh by means of bilinear interpolation. Thus, the five velocities

871    $u_2, u_4, u_5, u_6, u_8$ are obtained in terms of vertex velocities $u_1, u_3, u_7, u_9$, and similarly for the

872    $w$ velocities. The resulting complete set of fine mesh variables is used calculate the

873    divergence $D = \left(\partial u/\partial x + \partial w/\partial z\right)$ and the quantity $\partial w/\partial x$ in each of the eight triangular

874    elements $t_1, t_2, \cdots, t_8$ of the fine mesh. Coarse mesh pressures $\tilde{P}_1, \tilde{P}_2$ are associated with

875    the coarse mesh triangles $T_1, T_2$. The products $\tilde{P}_1 D$ in elements $t_1, t_2, t_3, t_5$ and $\tilde{P}_2 D$ in

876    elements $t_4, t_6, t_7, t_8$ are then accumulated over the entire mesh to obtain the quantity

877    $\tilde{P}\left(\partial u/\partial x + \partial w/\partial z\right)$ for use in the transformed functional $\tilde{\mathcal{A}}$. Similarly, the quantity

878    $\partial w/\partial x$ is computed in the fine mesh elements from coarse mesh variables for use in the

879    second invariant $\tilde{\dot{\varepsilon}}^2$.

880

881 (2) Approximation B, Linear interpolation:

882       In this version, the three velocities at the vertices of the two coarse mesh triangles

883 $T_1$ and $T_2$, i.e., $u_1, u_3, u_7$ and $w_1, w_2, w_3$ in $T_1$, and $u_7, u_3, u_9$ and $w_3, w_2, w_4$ in $T_2$,

884 approximate the divergence $D = \left( \partial u / \partial x + \partial w / \partial z \right)$ and $\partial w / \partial x$ as constant values in the

885 two coarse triangles. The constant values $\tilde{P}_1 D$, $\tilde{P}_2 D$ are then accumulated over the

886 entire mesh. The constant value $\partial w / \partial x$ in each coarse triangle is then distributed to each

887 of the eight fine mesh elements $t_1, t_2, \cdots, t_8$, depending on whether the centroid of the fine

888 triangular element is in $T_1$ or $T_2$. As in the previous case, this is then used in the second

889 invariant $\tilde{\tilde{\varepsilon}}^2$ in the transformed functional $\tilde{\tilde{A}}$.

890
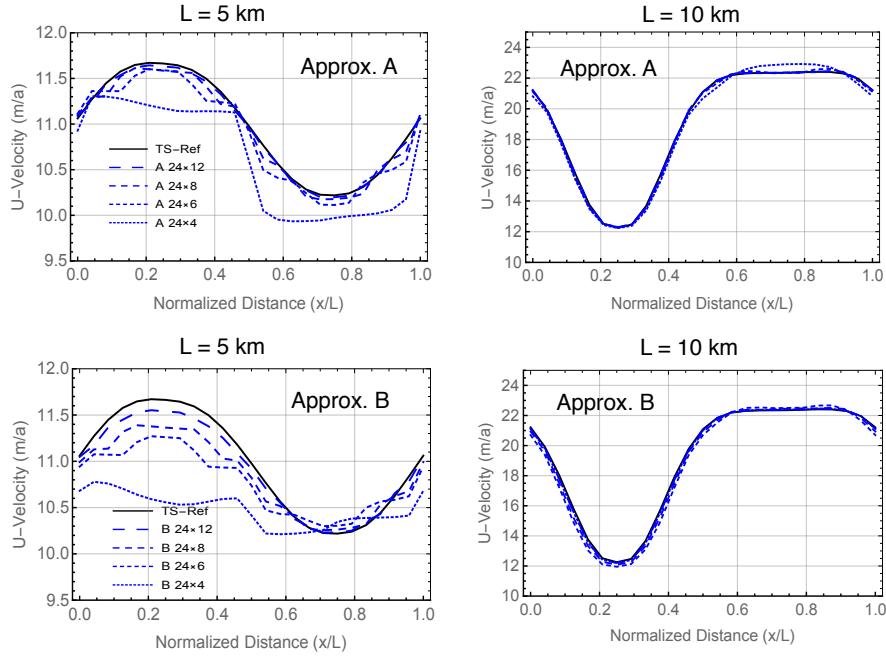
891     **Figure 11.** Comparing Approximations A and B. Test B. Upper surface u-velocity.

892     TS-Ref: Ref. Stokes (r x r = 24x24); Fine/Coarse resolutions (r x R = 24x12, 8, 6, 4).

893

894       While the number and type of unknown variables is the same in the two versions,

895 they differ considerably in accuracy as seen in Figs. 11 and 12. Fig. 11 compares the

896 upper surface u-velocity in approximations A and B, for the five mesh combinations, to

897 the reference 24x24 fine mesh transformed Stokes (TS) calculation. The corresponding

898 Blatter-Pattyn result is shown in Fig. 9. Fig. 12 summarizes and compares the overall

899 accuracy of all approximations by means of the RMS u-Error relative to the TS

May 17, 2025

900    calculation. As might be expected, the accuracy of Approx. A is better than Approx. B,

901    particularly in the case $L = 10$ km. Both dual-mesh versions are more accurate than the

902    BP and H approximations, except for the lowest 24x4 resolution of Approx. B. However,

903    it may be surprising that the SS calculation is the least accurate but this is because SS is

904    not yet fully converged at this resolution (see Fig. 5).

905
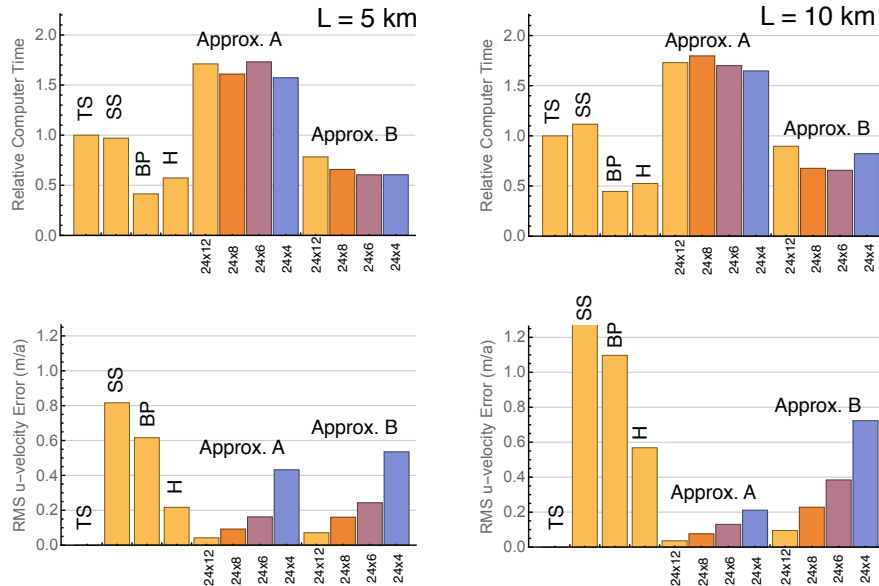
906    **Figure 12.** Comparing the Test B computer time and RMS u-Error results relative

907        to a TS calculation for Approximations BP, H, A, B, and the SS Stokes model.

908        TS, SS, BP, H: Resolution (r x r = 24x24); Approx. A, B: (r x R = 24x12, 8, 6, 4).

909

910        A qualitative comparison of computational time relative to the TS calculation is

911    presented in Fig. 12 for the 24x24 resolution case. The cost of the BP approximation is

912    substantially lower than the cost of full Stokes, while the cost of the Herterich

913    approximation is only slightly higher than BP. This comparison is qualitative and rough

914    because the present calculations are not at all representative of the computer hardware or

915    the methods used in practical ice sheet modeling. The calculations are proof of concept

916    only, made on a personal computer using the program Mathematica, a slow interpreted

917    language. As a result the cost comparisons are inaccurate and possibly misleading. No

918    effort was made to optimize the calculations or to take advantage of parallelization.

919    Thus, for example, the cost of dual-mesh approximations A and B is greatly affected by

920    the cost of the associated interpolations, making them more costly than even the

921    unapproximated calculations, TS and SS. However, the interpolations are highly

922    parallelizable and so would contribute little to the cost in practical computations.

923

924 **7. Second-Order Discretizations**

925

926 So far we have used first-order elements, primarily P1-E0. However, in current practice

927 Stokes models are more often based on second-order elements such as the popular

928 Taylor-Hood P2-P1 element (e.g., Leng et al., 2012; Gagliardini et al., 2013). In 2D the

929 P2-P1 element, illustrated in Fig. 13A, has velocities on element vertices and edge

930 midpoints and pressures on element vertices, resulting in quadratic velocity and linear

931 pressure distributions. This element satisfies the inf-sup stability condition (e.g., Elman

932 et al., 2014) but does not satisfy the solvability condition (58). For example, Test B with

933 direct substitution for basal boundary conditions requires $n_w = 4nm$ vertical velocity

934 variables, many more than the $n_p = n(m+1)$ pressure variables.

935

936      Stokes models work well with a Taylor-Hood mesh as shown in Fig. 13 where

937 both the P2-P1 and P1-E0 models converge to a common Test B solution. Recall that the

938 P2-P1 mesh does not work with the extended Blatter-Pattyn approximation, a model that

939 requires the solvability condition. However, it is possible to construct a second-order

940 element consistent with an invertible continuity equation. This is the P2-E1 element, as

941 illustrated in Fig. 13A. This is second-order for velocities and linear for pressure, just

942 like the P2-P1 element, but the pressure is edge-based rather than vertex-based.

943 Pressures are located midway between velocities along vertical lines, as illustrated in Fig.

944 13A. As explained in Appendix A, this mesh must be constructed using vertical columns

945 of quadrilaterals. Since pressures are vertically collinear with velocities, as in the P1-E0

946 element, the analysis in Appendix A confirms that this element also satisfies the

947 solvability condition (58). A 3D analog exists as is explained in Appendix A.

948

949      Fig. 13B shows the approximate error of the ice transport as a function of mesh

950 refinement for the second-order P2-P1 and P2-E1 meshes in transformed Stokes Test B

951 calculations, together with similar results for the first-order P1-E0 mesh from Fig. 3, for

952 comparison. Note that both second order models show approximately the same error at

953 resolution $r = 16$ as the first order P1-E0 model at resolution $r = 40$, and the same for

954 coarser resolutions such as $r = 8$ and $r = 20$, respectively. However, the second-order

955 calculations are considerably more expensive than the first-order calculations at

956 comparable resolution or accuracy.

May 17, 2025

957
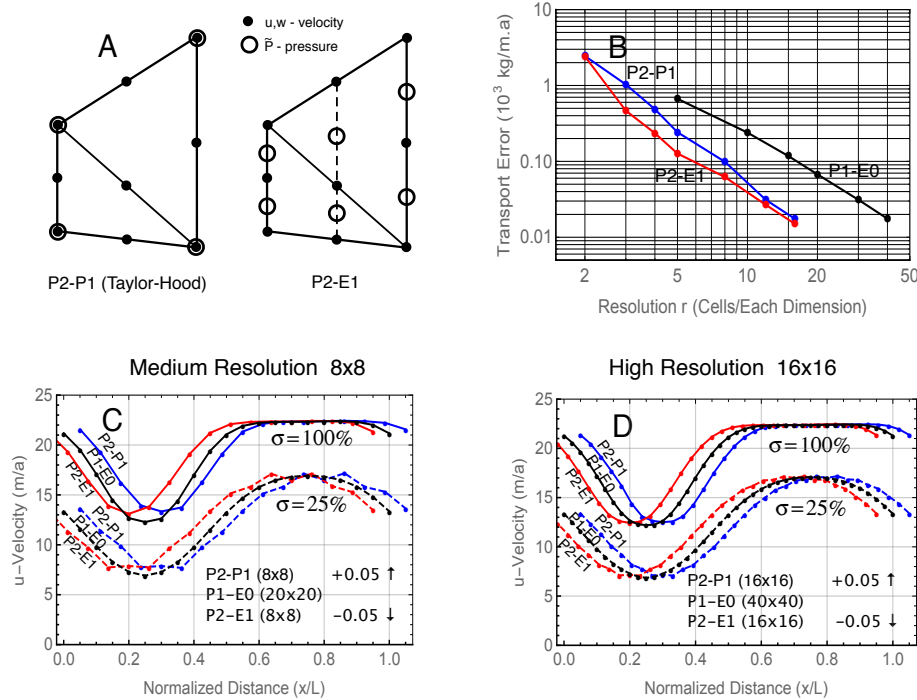
958 **Figure 13.** Comparing second-order discretizations based on the P2-P1 and P2-E1

959 elements from panel A to first-order discretizations using the P1-E0 element in Test B

960 calculations with L=10 km. Only transformed Stokes calculations are compared;

961 standard Stokes results behave similarly. Panel B compares the convergence and

962 accuracy of various schemes with increasing resolution, while panels C, D compare

963 horizontal velocities at medium and maximum resolutions.

964

965       Panels C, D in Fig. 13 compare u-velocities from several Test B calculations

966 using the two second-order models to the first-order P1-E0 model results from Fig. 3.

967 Each panel shows upper surface velocities ($\sigma = 100\%$) in solid lines and velocities from

968 a surface a quarter of the way up from the bottom ($\sigma = 25\%$) in dashed lines. Panel C

969 shows medium resolution calculations ($r = 8, 20$ in the second-order and first-order

970 calculations, respectively) and panel D shows higher resolution calculations ($r = 16, 40$).

971 At these resolutions the accuracy of the first- and second-order calculations is very

972 similar so for clarity the second-order results are displaced horizontally from the first-

973 order results by 0.05 nondimensional units. The P2-E1 results in magenta are displaced

974 to the left and the P2-P1 results in blue are displaced to the right. In general, models that

975 satisfy the solvability condition, the P1-E0 and P2-E1 models, are better behaved than the

976 P2-P1 model. This may be related to the well-known "weak" mass conservation of the

977 Taylor-Hood element, which is greatly improved by "enriching" the pressure space with

978    constant pressures in each triangular element (Boffi et al., 2012). Thus, in the 2D Test B

979    problem the pressure variables increase from $n_p = n(m+1)$ in the basic Taylor-Hood

980    element to $n(3m+1)$, much closer to the $4nm$ needed to satisfy the solvability condition.

981    However, pressure in the P2-E1 case is highly oscillatory but well behaved in the P2-P1

982    case. This is consistent with the discussion in Appendix B since the P2-P1 mesh satisfies

983    the inf-sup condition, which is concerned with regularizing the pressure solution (i.e., a

984    condition on the $\mathbf{B}^T$ matrix), while the P2-E1 mesh has no such requirement.

985

986    **8. A Summary and Discussion**

987

988    In summary, this paper presents two innovations in ice sheet modeling. The first involves

989    a transformation of the ice sheet Stokes equations into a form that differs from the

990    approximate Blatter-Pattyn system by a small number of terms. In particular, the

991    variational formulations differ only by the absence of terms involving the vertical

992    velocity $w$ in the second invariant of the strain rate tensor in the Blatter-Pattyn system.

993

994        We focus on two applications of the new transformation, although others may be

995    possible. The first allows these extra terms to be "switched" on or off to convert the code

996    from a full-Stokes model to a Blatter-Pattyn model if desired. Ice sheet flow is generally

997    shallow but often contains limited areas where Stokes equations must be solved. Thus,

998    the switch from Blatter-Pattyn to Stokes may be done locally and adaptively only where

999    the extra accuracy is required.

1000

1001        The fact that neglecting the vertical velocity in only one localized place creates

1002    the Blatter-Pattyn approximation suggests that an improved approximation will result

1003    from approximating rather than neglecting the vertical velocity. We present two such

1004    approximations but again others may be possible. The first approximation solves the

1005    pressure-free horizontal momentum equation with the vertical velocity obtained from the

1006    continuity equation. This approximation turns out to be the same as a model originally

1007    developed by Herterich (1987). We therefore refer to it as the Herterich approximation.

1008    The second approximation is obtained by discretizing the continuity equation on a coarser

1009    mesh than that used by the rest of the model, which yields an approximate vertical

1010    velocity and thus an approximate Stokes model.

1011

1012    The second innovation introduces the use of finite element discretizations that
1013 create a decoupled invertible continuity equation. This allows for the numerical solution
1014 of the vertical velocity in terms of the horizontal velocity components, i.e., $w = w(u,v)$.
1015 These meshes are a prerequisite for the applications mentioned above. Examples of such
1016 meshes for use in 2D and 3D are given in Appendix A, including the P1-E0 mesh that is
1017 used in most of the test problems of this paper. However, perhaps the most important
1018 consequence of this is that invertibility of the continuity equation serves as an alternative
1019 condition for the well posedness of Stokes saddle point problems, as explained in
1020 Appendix B.
1021
1022 **Code Availability**
1023
1024 All calculations were made using the Wolfram Research, Inc. program Mathematica in a
1025 development environment. A large number of Mathematica Notebooks were used to
1026 produce the various results. A representative Notebook (a ,nb file) is available in a public
1027 repository at https://doi.org/10.5281/zenodo.13940989 for a Test $D^*$ calculation
1028 (described in Appendix C) at $L = 10\,\text{km}$ and a resolution of 20x20. This test problem
1029 was chosen to demonstrate the use of direct substitution for the frictional tangential
1030 boundary condition, (16), in the functional. A Mathematica Notebook may be viewed by
1031 downloading the free Wolfram Player from https://www.wolfram.com/player/. However,
1032 the full Mathematica code is required for editing or execution.
1033
1034 **Competing Interests**
1035
1036 The author has acknowledged that there are no competing interests.
1037
1038 **Acknowledgements**
1039
1040 I am grateful to Steve Price for support, and especially to Mauro Perego, William (Bill)
1041 Lipscomb, and reviewers, particularly Christian Schoof, for comments and suggestions
1042 that helped to improve the paper.
1043

May 17, 2025

**References**

Auricchio, F., da Veiga, L.B., Brezzi, F., and Lovadina, C.: Mixed Finite Element Methods, In Encyclopedia of Computational Mechanics Second Edition (Eds E. Stein, R. de Borst, and T.J.R. Hughes), John Wiley & Sons, Ltd., 2017.

Benzi, M., Golub, G.H., and Liesen, J.: Numerical Solution of Saddle Point Problems, Acta Numerica, 14 , 1-137, doi:10.1017/S0962492904000212, 2005.

Blatter, H.: Velocity and Stress Fields in Grounded Glaciers: A Simple Algorithm for Including Deviatoric Stress Gradients, J. Glaciol., 41, 333-344, 1995.

Boffi, D., Brezzi, F., Fortin, M.: Finite Elements for the Stokes Problem. In: Boffi D., Gastaldi L. (eds) Mixed Finite Elements, Compatibility Conditions, and Applications. Lecture Notes in Mathematics, vol 1939. Springer, Berlin, Heidelberg. https://doi.org/10.1007/978-3-540-78319-0_2, 2008.

Boffi, D., Cavallini, N., Gardini, F., and Gastaldi, L.: Local Mass Conservation of Stokes Finite Elements, J. Sci. Comput., 52, 383–400, 2012.

Cheng, G., Lötstedt, P., and von Sydow, L.: A Full Stokes Subgrid Scheme in Two Dimensions for Simulation of Grounding Line Migration in Ice Sheets Using Elmer/ICE (v8.3), Geosci. Model Dev., 13, 2245-2258, 2020.

Colinge, J., and Rappaz, J.: A Strongly Nonlinear Elliptic Problem Arising in a Non-Newtonian Fluid Flow Model in Glaciology, Math. Model. Numer. Anal., 33, 395-406,1999.

Dukowicz, J.K., Price, S.F., and Lipscomb, W.H.: Consistent Approximations and Boundary Condition for Ice Sheet Dynamics from a Principle of Least Action, J. Glaciol., 56, 480-496, 2010.

May 17, 2025

1076 Dukowicz, J.K., Price, S.F., and Lipscomb, W.H.: Incorporating Arbitrary Basal
1077 Topography in the Variational Formulation of Ice Sheet Models, J. Glaciol., 57, 461-467,
1078 2011.
1079
1080 Elman, H.C., Silvester D.J., and Wathen A.J.: Finite Elements and Fast Iterative Solvers:
1081 With Applications in Incompressible Fluid Dynamics, 2nd Ed., Oxford University Press,
1082 494 pp, 2014.
1083
1084 Gagliardini, O., and Zwinger, T.: The ISMIP-HOM Benchmark Experiments Performed
1085 Using the Finite-Element Code Elmer, The Cryosphere, 2, 67–76, 2008.
1086
1087 Gagliardini, O., Zwinger, T., Gillet-Chaulet. F., Durand, G., Favier, L., de Fleurian, B.,
1088 Greve, R., Malinen, M., Martín, C., Råback, P., Ruokolainen, J., Sacchettini, M., Schäfer,
1089 M., Seddik, H., and Thies, J.: Capabilities and Performance of Elmer/Ice, a New-
1090 Generation Ice Sheet Model, Geosci. Model Dev., 6, 1299–1318, doi:10.5194/gmd-6-
1091 1299-2013, 2013.
1092
1093 Gerbeau, J-F.: Finite Elements for Mixed and Saddle Point Problems, Chapter 3 (in
1094 particular Remarks 3.2 and 3.3), Course CME358, Stanford University,
1095 https://web.stanford.edu/class/cme358/handouts.html, 2025.
1096
1097 Greve, R. and Blatter, H.: Dynamics of Ice Sheets and Glaciers, Springer-Verlag, Berlin
1098 Heidelberg, 301 pp, 2009.
1099
1100 Heinlein, A., Perego, M., and Rajamanickam, S.: FROSch Preconditioners for Land Ice
1101 Simulations of Greenland and Antarctica, SIAM J. Sci. Comput., 44, V339-B367, doi:
1102 10.1137/21M1395260, 2022.
1103
1104 Herterich, K.: On the Flow Within the Transition Zone Between Ice Sheet and Ice Shelf,
1105 in Dynamics of the West Antarctic Ice Sheet, Proceedings of a workshop held in Utrecht,
1106 May 6-8, 1985, (Eds. C. J. Van Der Veen and J. Oerlemans), D. Reidel, Dordrecht, 185-
1107 202, 1987.
1108
1109 Hoffman, M. J., Perego, M., Price, S. F., Lipscomb, W. H., Zhang, T., Jacobsen, D.,

1110    Tezaur, I., Salinger, A. G., Tuminaro, R., and Bertagna, L.: MPAS-Albany Land Ice

1111    (MALI): A Variable-Resolution Ice Sheet Model for Earth System Modeling Using

1112    Voronoi Grids, Geosci. Model Dev., 11, 3747–3780, doi:10.5194/gmd-11-3747-2018,

1113    2018.

1114

1115    Hood, P. and Taylor, C.: Numerical Solution of the Navier-Stokes Equations Using the

1116    Finite Element Technique, Comput. Fluids, 1, 1-28, 1973.

1117

1118    Larour, E., Seroussi, H., Morlighem, M., and Rignot, E.: Continental scale, high order,

1119    high spatial resolution, ice sheet modeling using the Ice Sheet System Model (ISSM), J.

1120    Geophys. Res., 117, 1–20, doi:10.1029/2011JF002140, 2012.

1121

1122    Leng, W., Ju, L., Gunzburger, M., Price, S., and Ringler, T.: A Parallel High-Order

1123    Accurate Finite Element Nonlinear Stokes Ice Sheet Model and Benchmark Experiments,

1124    J. Geophys. Res., 117, 2156–2202, doi:10.1029/2011JF001962, 2012.

1125

1126    Lipscomb, W.H., Price, S.F., Hoffman, M.J., Leguy, G.R., Bennett, A.R., Bradley, S.L.,

1127    Evans, K.J., Fyke, J.G., Kennedy, J.H., Perego, M., Ranken, D.M., Sacks, W.J., Salinger,

1128    A.G., Vargo, L.J., and Worley, P.H.: Description and Evaluation of the Community Ice

1129    Sheet Model (CISM) v. 2.1, Geosci. Model Dev., 12, 387-424, 2019.

1130

1131    Nowicki, S.M.J. and Wingham, D.J.: Conditions for a Steady Ice Sheet-Ice Shelf

1132    Junction, *Earth Planet. Sci. Lett.*, **265**(1-2), 246-255, 2008.

1133

1134    Pattyn, F.: A New Three-Dimensional Higher-Order Thermomechanical Ice Sheet

1135    Model: Basic Sensitivity, Ice Stream Development, and Ice Flow across Subglacial

1136    Lakes, J. Geophys. Res., 108(B8), 2382, 2003.

1137

1138    Pattyn, F., Perichon, L., Aschwanden. A., Breuer, B., de Smedt, B., Gagliardini, O.,

1139    Gudmundsson, G.H., Hindmarsh, R.C.A., Hubbard, A., Johnson, J.V., Kleiner, T.,

1140    Konovalov, Y., Martin, C., Payne, A.J., Pollard, D., Price, S., Ruckamp, M., Saito, F.,

1141    Soucek, O., Sugiyama, S., and Zwinger, T.: Benchmark Experiments for Higher-Order

1142  and Full-Stokes Ice Sheet Models (ISMIP–HOM*),* The Cryosphere, 2, 95-108, 2008.

1143

1144  Perego, M., Gunzburger. M., and Burkardt, J.: Parallel Finite-Element Implementation

1145  for Higher-Order Ice-Sheet Models, J. Glaciol., 58, 76-88, 2012.

1146

1147  Rappaz, J., and Reist, A.: Mathematical and Numerical Analysis of a Three-Dimensional

1148  Fluid Flow Model in Glaciology, Math. Model. Mech. Appl. Sci., 15, 37-52, 2005.

1149

1150  Rückamp, M., Kleiner, T., and Humbert, A.: Comparison of ice dynamics using full-

1151  Stokes and Blatter-Pattyn approximation: application to the Northeast Greenland Ice

1152  Stream, The Cryosphere, 16, 1675-1696, 2022.

1153

1154  Schoof, C.: A Variational Approach to Ice Stream Flow, J. Fluid Mech., 556, 227-251,

1155  2006.

1156

1157  Schoof, C.: Coulomb friction and other sliding laws in a higher order glacier flow model,

1158  Math. Models. Meth. Appl. Sci., 20(1), 157–189, 2010.

1159

1160  Schoof, C. and Hewitt, I.: Ice-Sheet Dynamics, Annu. Rev. Fluid Mech., 45, 217–239,

1161  2013.

1162

1163  Schoof, C. and Hindmarsh, R.C.A.: Thin-Film Flows with Wall Slip: An Asymptotic

1164  Analysis of Higher Order Glacier Flow Models, Quart. J. Mech. Appl. Math, 63, *73-114*,

1165  2010.

1166

1167  Seroussi, H., Ben Dhia, H., Morlighem, M., Latour, E., Rignot, E., and Aubry, D.:

1168  Coupling Ice Flow Models of Varying Orders of Complexity with the Tiling Method, J.

1169  Glaciol., 58, 776-786, 2012.

1170

1171  Tezaur, I. K, Perego, M., Salinger, A. G., Tuminaro, R. S., and Price, S. F.:

1172  Albany/FELIZ: A Parallel, Scalable and Robust, Finite Element, First-Order Stokes

1173  Approximation Ice Sheet Solver Built for Advanced Analysis, Geosci. Model Dev., 8,

1174  1197-1220, 2015.

1175

1176 **Appendix A: Meshes that Satisfy the Solvability Condition**

1177 **A1 The P1-E0 Element and the Invertibility of the Continuity Equation**

1178

1179 As discussed in §4, the invertibility of the discrete continuity equation requires special

1180 elements and meshes that satisfy the solvability condition (58). The P1-E0 element,

1181 illustrated in Fig. A1, is one such triangular element that has been used on many

1182 problems in this paper. To work best for the purpose of inverting the continuity equation

1183 for the vertical velocity, i.e., (56), it must be used in a mesh composed of vertical

1184 columns subdivided into triangular elements as shown in a representative mesh in Fig.

1185 A2. Element P1-E0 has velocities located at triangle vertices for a linear velocity

1186 distribution within each triangle (P1), and pressure located on the vertical edge of each

1187 triangle for a constant pressure distribution over the two triangles that share the edge

1188 (E0). A second order version of this element, the P2-E1 element, is shown in Fig. 13A.

1189
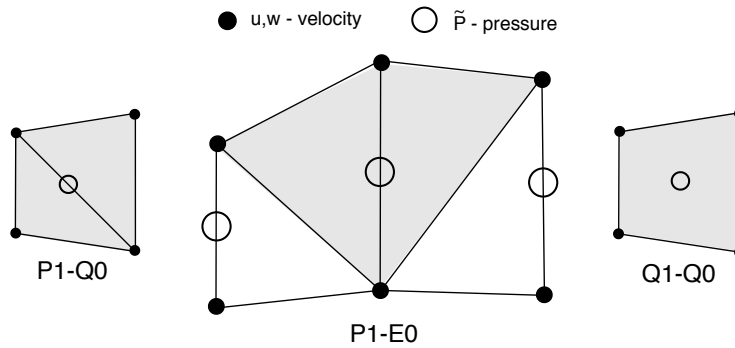
1190 **Figure A1.** The P1-E0 element, and two other secondary 2D elements that satisfy

1191 the solvability condition but possibly only in Tests B and D*.

1192

1193 The triangulation and configuration of pressure basis functions (shown in gray) in

1194 Fig. A2 is quite general except that elements must be arranged in vertical columns, which

1195 still allows for a flexible triangulation of an arbitrary domain. Generally, there are two

1196 triangles associated with a pressure variable, one on each side of a vertical edge, except

1197 where the ice sheet ends at a vertical face, as in Fig. A2. However, this is not a problem

1198 since the pressure is simply associated with the single triangle on one side of the vertical

1199 face. Meshes composed of P1-E0 elements have another useful property. Since pressure

1200 and vertical velocity variables alternate along vertical mesh lines, the matrix-vector

1201 products $\mathbf{M}_{WP}p$, $\mathbf{M}_{WP}^{T}w$ in (46), corresponding to $\partial\tilde{P}/\partial z$ and $\partial w/\partial z$ in the vertical

1202 momentum and continuity equations, respectively, consist of simple decoupled bi-

1203 diagonal one-dimensional difference equations along each vertical mesh line for

1204   determining pressure and vertical velocity. This will be particularly advantageous for

1205   parallelization.

1206
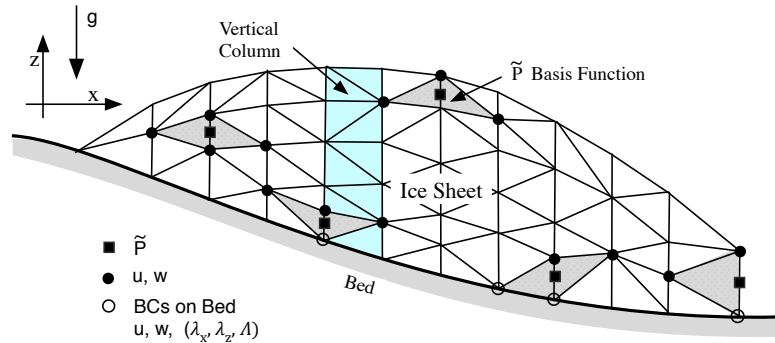
1207   **Figure A2.** An illustration of a 2D edge-based P1-E0 mesh, composed of

1208   vertical columns randomly subdivided into triangles.

1209

1210   The other two elements shown in Fig. A1, the P1-Q0 and Q1-Q0 elements, satisfy

1211   the solvability condition when used in Tests B and D* but possibly not in other problems.

1212   The P1-Q0 element has velocities on triangle vertices for a linear velocity distribution

1213   within each triangle (P1) but pressure is constant within the quadrilateral (Q0) formed by

1214   the two adjoining triangles. The Q1-Q0 element has velocities located at quadrilateral

1215   vertices and pressure centered in the quadrilateral, resulting in a bi-quadratic velocity

1216   distribution (Q1) and a constant pressure within the quadrilateral (Q0). Solutions for all

1217   three elements are stable as expected, and they converge to the same value for ice

1218   transport. The pressure distribution is smooth in the P1-E0 case but contains small

1219   fluctuations near the upper surface in the P1-Q0 and Q1-Q0 cases. These disappear as

1220   resolution is increased. The Q1-Q0 element is unstable in conventional applications

1221   because it contains a checkerboard pressure null space and is only used in a stabilized

1222   form (see Elman et al., 2014, where the element is called Q1-P0). Here, however, it

1223   behaves well perhaps because it satisfies the solvability condition. Overall, this confirms

1224   our expectation of stability when the solvability condition is satisfied.

1225

1226   **A2 Proving the Solvability Condition in P1-E0 Element Meshes**

1227

1228   Consider a single vertical edge from top to bottom as in Fig. A2. Assuming

1229   there are $m$ edge segments in the vertical direction, there will be $m+1$ discrete $w$

1230   variables and $m$ discrete $\tilde{P}$ variables since each $\tilde{P}$ variable is located between a pair of

1231   $w$ variables. However, since the $w$ variable at the bottom (the bed) is specified as a

1232   boundary condition, either directly as a no-slip condition or as part of a no-penetration

1233    condition, there will be only $m$ unknown $w$ variables. As a result, we have $n_w = n_p$

1234    along each vertical mesh edge and therefore over the entire mesh, thus satisfying the

1235    solvability condition. In case Lagrange multipliers are used, there will be $m+1$ unknown

1236    discrete $w$ variables (since now the basal vertical velocity $w$ is also an unknown).

1237    However, this is matched by $m$ unknown $\tilde{P}$ variables, supplemented by one $\lambda_z$ or one

1238    $\Lambda$ unknown Lagrange multiplier variable, depending on the type of boundary condition.

1239    Thus, again the number of unknown variables equals the number of equations along

1240    every vertical edge, thereby satisfying the solvability condition. This means that the P1-

1241    E0 element can be used to satisfy the solvability condition irrespective of the boundary

1242    conditions on quite arbitrary meshes. These arguments apply to other versions of the P1-

1243    E0 element as well, such as the second order version P2-E1 in Fig. 13A or the 3D version

1244    in Fig. A3.

1245

1246    **A3 Three-Dimensional Meshes Based on the P1-E0 Element**

1247

1248    The two-dimensional P1-E0 element has a relatively simple three-dimensional

1249    counterpart, shown in Fig. A3. The mesh again consists of vertical columns, this time

1250    composed of hexahedra. Each hexahedron is subdivided into six tetrahedra such that

1251    each vertical edge is surrounded by as few as four to as many as eight tetrahedra. As in

1252    the 2D case, velocity components are collocated at vertices, yielding a piecewise-linear

1253    velocity distribution in each tetrahedral element, and pressures are located in the middle

1254    of each vertical edge so that pressure is constant in the collection of tetrahedra that

1255    surround that edge. Lagrange multipliers, if used, are located at the vertices on the basal

1256    surface, yielding a piecewise linear distribution on the basal triangular facet. Since

1257    pressures and vertical velocities are again intermingled along a single line of vertical

1258    edges from top to bottom, this satisfies the solvability condition (58) because the

1259    argument used in the 2D case applies here also.

1260

1261    Fig. A3 shows two of the several possible configurations of a typical hexahedron,

1262    including an exploded view of each configuration for clarity. The two configurations

1263    differ in having the internal face of the two forward-facing tetrahedra rotated, creating

1264    two different forward facing tetrahedra. The remaining six tetrahedra are undisturbed.

1265    Since edges must align when hexahedra (or tetrahedra) are connected, this shows that the

1266    3D mesh can be flexibly reconnected and rearranged, just as in the 2D case of Fig. A2.

1267

May 17, 2025

1268    A closely related and perhaps simpler three-dimensional P1-E0 element is based
1269    on the P2-P1 prismatic tetrahedral element in Leng et al. (2012).  A mesh of these
1270    elements is composed of vertical columns of prisms (with triangular faces at the top and
1271    bottom), each subdivided into three tetrahedra.  Pressures are located on the vertical
1272    prism edges, as in Fig. A3, so this again satisfies the solvability condition.
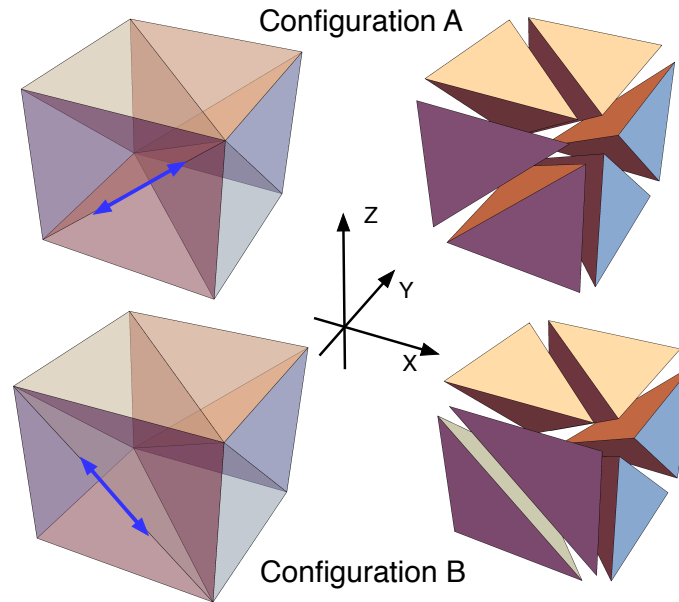
1273
1274    **Figure A3.** Three-dimensional P1-E0 tetrahedral elements that generalize the 2D P1-E0
1275        element of Fig. A1.  Configurations A and B differ by having an internal triangular
1276        face rotated, as indicated by the blue arrows.  Both satisfy the solvability condition.
1277
1278    Just as the 2D second-order P2-E1 element in Fig. 13A is a generalization of the
1279    P1-E0 element, a 3D second-order P2-E1 element may be constructed as a generalization
1280    of the P1-E0 element in Fig. A3.  Velocities would be located at the vertices and at
1281    midpoints of the tetrahedral edges, and pressures halfway between the velocities on
1282    vertical edges, including the imaginary vertical edges through the midpoints of the
1283    tetrahedral edges as in the 2D case in Fig. 13A.  The P2-E1 element in both 2D and 3D
1284    satisfies the solvability condition since the arguments of §B2 also apply here as pressures
1285    are located midway between vertical velocities along all vertical edges.
1286

1287 **Appendix B: The Inf-Sup and Solvability Conditions**

1288

1289 Recalling (47), the 2D Newton-Raphson iteration for saddle point problems is written as

1290
$$\begin{bmatrix} \mathbf{M}_{UU}\left(u^K,w^K\right) & \mathbf{M}_{UW}\left(u^K,w^K\right) & \mathbf{M}_{UP} \\ \mathbf{M}_{UW}^T\left(u^K,w^K\right) & \mathbf{M}_{WW}\left(u^K,w^K\right) & \mathbf{M}_{WP} \\ \mathbf{M}_{UP}^T & \mathbf{M}_{WP}^T & 0 \end{bmatrix} \begin{Bmatrix} \Delta u \\ \Delta w \\ \Delta p \end{Bmatrix} = \begin{Bmatrix} -R_U\left(u^K,w^K,p^K\right) \\ -R_W\left(u^K,w^K,p^K\right) \\ 0 \end{Bmatrix}. \quad (71)$$

1291 In the 3D case the vector $\Delta u$ may stand for the vector of horizontal variable increments,

1292 i.e., $\left\{\Delta u, \Delta v\right\}^T$. For simplicity, dropping the $\Delta$'s and renaming quantities, (71) is put in

1293 the standard form (54), as follows

1294
$$\begin{bmatrix} \mathbf{A} & \mathbf{B}^T \\ \mathbf{B} & 0 \end{bmatrix} \begin{Bmatrix} \mathbf{u} \\ p \end{Bmatrix} = \begin{Bmatrix} \mathbf{f} \\ g \end{Bmatrix}, \quad (72)$$

1295 where $\mathbf{u} = \left\{u,w\right\}^T$, $\mathbf{A} = \begin{bmatrix} \mathbf{M}_{UU}\left(u^K,w^K\right) & \mathbf{M}_{UW}\left(u^K,w^K\right) \\ \mathbf{M}_{UW}^T\left(u^K,w^K\right) & \mathbf{M}_{WW}\left(u^K,w^K\right) \end{bmatrix}$, $\mathbf{B} = \begin{bmatrix} \mathbf{M}_{UP}^T & \mathbf{M}_{WP}^T \end{bmatrix}$, etc.,

1296 and the correspondences of the other variables should be obvious.

1297

1298 As noted earlier, matrix $\mathbf{A}$ is invertible. Eliminating $\mathbf{u}$ in (72), we obtain an

1299 equation for the pressure,

1300
$$\left(\mathbf{B}\mathbf{A}^{-1}\mathbf{B}^T\right)p = \left(\mathbf{B}\mathbf{A}^{-1}\right)\mathbf{f}, \quad (73)$$

1301 where $\mathbf{S} = \left(\mathbf{B}\mathbf{A}^{-1}\mathbf{B}^T\right)$ is called the Schur complement with respect to $p$. This equation

1302 may be solved for $p$ provided an inf-sup condition on matrix $\mathbf{B}^T$ is satisfied (Benzi et

1303 al., 2005; Gerbeau, 2025). Having solved for $p$, the equation to be solved for velocity is

1304
$$\mathbf{A}\mathbf{u} = \mathbf{f} - \mathbf{B}^T p. \quad (74)$$

1305 This is generally not attractive as a practical solution method since the Schur complement

1306 matrix $\mathbf{S}$ is full and therefore (73) too expensive to solve. However, Gerbeau (2025)

1307 points out that the standard inf-sup condition for $\mathbf{B}^T$ is equivalent to the much simpler

1308 "algebraic inf-sup condition",

1309
$$Ker\mathbf{B}^T = \left\{0\right\}, \quad (75)$$

May 17, 2025

1310      i.e., the inf-sup condition is the same as requiring that the null space of $\mathbf{B}^T$ be the zero

1311      vector. Further, this means that the inf-sup condition or (75) implies that the pressure

1312      solution must not contain spurious modes. Finally, this suggests that existence of a

1313      pressure null space is the culprit in the need to satisfy the inf-sup condition.

1314

1315      On the other hand, consider the situation when the Newton-Raphson system (71)

1316      is solved with a mesh satisfying the solvability condition. Simplifying notation, the

1317      linear system (71) may be rewritten as follows

1318
$$
\begin{bmatrix} \mathbf{M}_{UU} & \mathbf{M}_{UW} & \mathbf{M}_{UP} \\ \mathbf{M}_{UW}^T & \mathbf{M}_{WW} & \mathbf{M}_{WP} \\ \mathbf{M}_{UP}^T & \mathbf{M}_{WP}^T & 0 \end{bmatrix} \begin{Bmatrix} u \\ w \\ p \end{Bmatrix} = \begin{Bmatrix} f_U \\ f_W \\ 0 \end{Bmatrix} . \tag{76}
$$

1319      If the solvability condition applies, the matrices $\mathbf{M}_{WP}, \mathbf{M}_{WP}^T$ are invertible, as before, and

1320      the continuity equation, the third equation from (76), may be solved for the vertical

1321      velocity $w$ as before, as follows

1322
$$
w = -\mathbf{M}_{WP}^{-T}\mathbf{M}_{UP}^T u , \tag{77}
$$

1323      corresponding to (56). Recall from §4.3.2 that using (56) in functional (59) one obtains

1324      (60), an equation for $u$ only. With a bit of algebra, and now using (77) in (76), the

1325      corresponding linear equation for $u$ is given by

1326
$$
\left( \mathbf{M}_{UU} - \left( \mathbf{M}_{UW} - \mathbf{M}_{UP}\mathbf{M}_{WP}^{-1}\mathbf{M}_{WW} \right)\mathbf{M}_{WP}^{-T}\mathbf{M}_{UP}^T - \mathbf{M}_{UP}\mathbf{M}_{WP}^{-1}\mathbf{M}_{UW}^T \right) u
$$
$$
= \left( f_U - \mathbf{M}_{UP}\mathbf{M}_{WP}^{-1}f_W \right). \tag{78}
$$

1327      However, just as was the case with (73), the associated matrix is full and too expensive to

1328      solve in practice. Nevertheless, with $u$ given by (78), one obtains the following matrix

1329      equation from the second equation of (76), to be solved for the pressure $p$:

1330
$$
\mathbf{M}_{WP}p = \left( \mathbf{M}_{WW}\mathbf{M}_{WP}^{-T}\mathbf{M}_{UP}^T - \mathbf{M}_{UW}^T \right) u + f_W . \tag{79}
$$

1331      Thus, corresponding to equations (74) and (73), one obtains (78) and (79), but now to be

1332      solved in reverse order, first for velocity $u$, then for the pressure $p$. The essential

1333      difference between the equations for the pressure, (73) and (79), is that the Schur

1334      complement matrix $\mathbf{S}$ requires the inf-sup condition to be satisfied, while there is no such

1335      requirement for $\mathbf{M}_{WP}$ since it is an invertible matrix. Thus, pressure solutions will be

1336      well behaved with no spurious pressure modes, although there is no guarantee or

1337      expectation of smoothness. This implies that the solvability condition (58), and more

1338    importantly, the invertibility of matrix $\mathbf{M}_{WP}^{T}$, is sufficient for the well posedness of the

1339    Stokes saddle point problem.

1340

1341    **Appendix C: Test Problems**

1342

1343    We use three 2D test problems to demonstrate the new methods. The geometrical

1344    configuration of the three problem meshes is illustrated in Fig. C1. The first problem,

1345    named Test B, is actually Exp. B from the ISMIP-HOM benchmark suite (Pattyn et al.,

1346    2008); it features a no-slip condition on a sinusoidal basal surface. The second problem,

1347    Test D$^{*}$, incorporates sinusoidal friction along a uniformly sloped plane basal surface.

1348    This is a modification of Exp. D from the benchmark suite with increased friction since

1349    ice flow in Exp. D is very nearly vertically constant (see Fig. 4), which is characteristic of

1350    the shallow-shelf regime and not representative of a more typical flow regime.

1351

1352          A third problem, Test O (for "Obstacle") is introduced to illustrate the adaptive

1353    switching discussed in §6.1. As illustrated in Fig. C1, Test O has a unique feature, a thin

1354    no-slip obstacle, located at $x = 4 \, km$ and extending vertically $200 \, m$ from the bed (20 %

1355    of the ice sheet thickness), which forces ice flow near the obstacle to adjust abruptly.

1356    However, because of the no-slip boundary conditions along the obstacle surface, the

1357    triangular element in the lee of the obstacle, with one vertical edge and one edge along

1358    the bed, would result in zero vertex velocities. This would imply zero stress and

1359    therefore a singularity in ice viscosity. To avoid this, elements at the back of the obstacle

1360    are "reversed" compared to the ones at the front of the obstacle as shown in Fig. C1.

1361

1362          All tests feature a sloping flat upper surface, given by $z_{s}(x) = -x \operatorname{Tan}(\theta)$, where

1363    $\theta = 0.5°$ for Tests B and O, and $\theta = 0.3°$ for Test D$^{*}$ (this differs from the $0.1°$ slope in

1364    Test D), with free-stress boundary conditions. The bottom surface elevation in Test B is

1365    given by $z_{b}(x) = z_{s}(x) - H_{0} + H_{1} \operatorname{Sin}(\omega x)$, where the $H_{0} = 1000 \, m$, $H_{1} = 500 \, m$,

1366    $\omega = 2\pi / L$, and $L$ is the perturbation wavelength or domain length. The bottom surface

1367    elevation in Tests D$^{*}$ and O is $z_{b}(x) = z_{s}(x) - H_{0}$, which is parallel to the upper surface.

1368    Problem length $L$ in the ISMIP-HOM suite ranges from $5 \, km$ to $160 \, km$ but here we

1369    consider only three cases at the high end of the aspect ratio ($H_{0} / L$) range, namely

1370    $L = 2, 5, 10\ km$, where the inaccuracy of the Blatter-Pattyn approximation becomes

1371    noticeable. Lateral boundary conditions are periodic. The spatially varying friction

1372    coefficient for Test D* is $\beta(x) = \beta_0 + \beta_1 \mathrm{Sin}(\omega x)$, where $\beta_0 = \beta_1 = 10^4\ Pa\ a\ m^{-1}$ (this is

1373    an order of magnitude larger than in Test D). Physical parameters are the same as in

1374    ISMIP-HOM, i.e., ice-flow parameter $A = 10^{-16}\ Pa^{-3} a^{-1}$, ice density $\rho = 910\ kg\ m^{-3}$, and

1375    gravitational constant $g = 9.81\ ms^2$. In general, units are MKS, except usually time is

1376    per annum, convertible to per second by the factor $3.1557 \times 10^7\ s\ a^{-1}$.
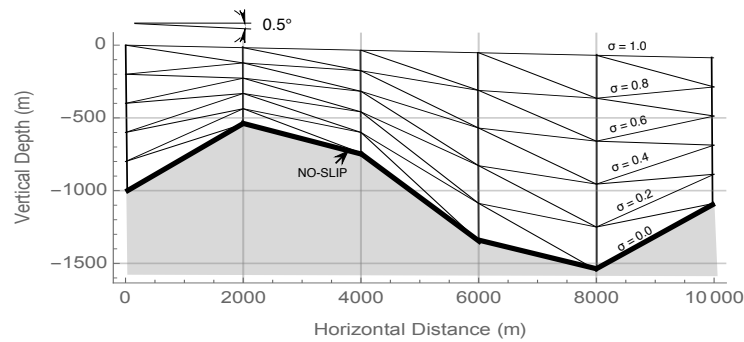
ISMIP-HOM Test Problem B - No Slip
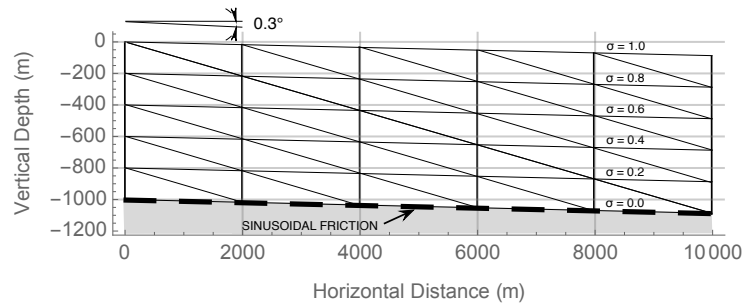
Test Problem D* - Sinusoidal Friction
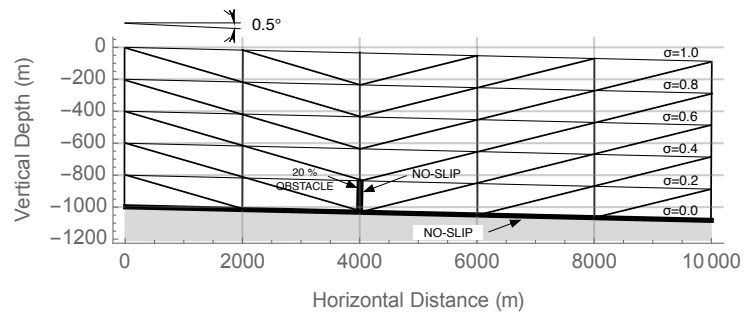
Test Problem O - 20% Obstacle - No Slip

1377

1378    **Figure C1.** Test problem meshes. For clarity, a coarse 5x5 configuration is shown.